

---

# Search for the ( $\Xi^0$ p) dibaryon with ALICE at the LHC

---

Master-Thesis von Joachim M. Tscheuschner  
March 2014



TECHNISCHE  
UNIVERSITÄT  
DARMSTADT

Fachbereich Physik  
Institut für Kernphysik,  
GSI Helmholtzzentrum für Schwerionen-  
forschung GmbH



ALICE

GSI



EMMI

Search for the ( $\Xi^0 p$ ) dibaryon with ALICE at the LHC

Vorgelegte Master-Thesis von Joachim M. Tscheuschner

1. Gutachten: Prof. Dr. P. Braun-Munzinger
2. Gutachten: Dr. M. Nicassio

Tag der Einreichung:

---

## Abstract

---

Dibaryons, bound states of two baryons, have been predicted for a long time. However, despite the effort on the experimental side, no other dibaryon than the deuteron has been found. Confirming their existence would give an insight into the interaction among baryons. At LHC energies they should have higher production probability since baryons and strange particles are abundantly produced and the ALICE apparatus, with its excellent particle identification and vertexing capabilities, is particularly suited to the search of these unstable states. In this thesis the investigation of the  $(\Xi^0 p)$  dibaryon [1] in Pb–Pb collisions at  $\sqrt{s_{NN}} = 2.76$  TeV is presented. It is predicted to weakly decay mainly in  $\Lambda + p$ . This decay, with  $\Lambda \rightarrow \pi^- + p$ , has a topology similar to the one of the multi-strange baryons already measured by the ALICE Collaboration [2–4]. In this work a Monte Carlo simulation, with a  $(\Xi^0 p)$  dibaryon mass of  $2.248 \text{ GeV}/c^2$  and a lifetime of  $c\tau = 7.8 \text{ cm}$ , is used to study the decay topology and the reconstruction efficiency. An invariant mass distribution of  $\Lambda$  and proton is built, no signal is observed. Therefor an upper limit to the production yield of the particle is estimated and compared to the thermal model prediction.



---

## Zusammenfassung

---

Dibaryonen, gebundene Zustände von zwei Baryonen, sind seit langem vorhergesagt. Trotz der Anstrengungen auf der experimentellen Seite, wurde bis heute kein anderes Dibaryon als das Deuteron gefunden. Die Observation eines solchen Zustandes würde einen tieferen Einblick in die Wechselwirkung zwischen den Baryonen geben. Bei den Energien, die mit dem LHC erreicht werden, sollte die Wahrscheinlichkeit der Formung eines solchen Zustandes hoch sein, weil Baryonen und Teilchen mit strangeness reichlich produziert werden. Die ALICE Apparatur ist mit ihren exzellenten Möglichkeiten zur Teilchenidentifikation und der guten Vertexauflösung bestens für die Suche nach Teilchen, die schwach zerfallen, geeignet. In dieser Arbeit wird die Suche nach dem Dibaryon ( $\Xi^0 p$ ) [1] in Pb–Pb Kollisionen bei einer Schwerpunktsenergie von  $\sqrt{s_{NN}} = 2.76$  TeV präsentiert. Das Dibaryon soll schwach hauptsächlich in ein  $\Lambda$  und proton zerfallen, die Zerfallskette, welche zur Rekonstruktion benutzt wird, lautet dann  $(\Xi^0 p) \rightarrow \Lambda + p \rightarrow p + \pi^- + p$ . Dieser Zerfall hat eine ähnliche Topologie wie die der geladenen Baryonen mit strangeness größer zwei,  $\Omega$  und  $\Xi$ , welche schon von der ALICE Kollaboration detektiert wurden [2–4]. In dieser Thesis wird eine Monte Carlo Simulation benutzt, um die Zerfallstopologie zu untersuchen und die Effizienz der Rekonstruktion des Dibaryons zu bestimmen. Die invariante Massenverteilung der Teilchen  $\Lambda$  und proton wird untersucht, in der kein Signal beobachtet wird, Daher wird eine obere Grenze für die Produktionsrate bestimmt und mit dem Thermal Model verglichen.



---

## Contents

---

<b>1</b>	<b>Introduction</b>	<b>7</b>
<b>2</b>	<b>Dibaryons</b>	<b>9</b>
2.1	Calculating dibaryon properties . . . . .	9
2.2	Thermal model . . . . .	10
2.3	Search for dibaryons . . . . .	12
<b>3</b>	<b>The Experiment</b>	<b>13</b>
3.1	The Large Hadron Collider . . . . .	13
3.2	The ALICE apparatus . . . . .	14
3.2.1	The Inner Tracking System . . . . .	15
3.2.2	The Time Projection Chamber . . . . .	15
3.2.3	The V0 detector . . . . .	16
3.2.4	Particle identification by energy loss . . . . .	16
3.2.5	Particle identification by weak decay topology . . . . .	17
<b>4</b>	<b>Analysis</b>	<b>21</b>
4.0.6	Event and Track selection . . . . .	21
4.1	Reconstruction strategy for the dibaryon . . . . .	22
4.2	Monte Carlo simulation study . . . . .	24
4.3	Results and discussion . . . . .	32
4.4	Effect of the lifetime on the efficiency . . . . .	37
<b>5</b>	<b>Conclusion and outlook</b>	<b>41</b>





---

## 1 Introduction

---

The theory of quantum chromodynamics (QCD) describes the strong interactions among quarks and gluons. Deriving from this fundamental theory the structure, properties, and interactions between more complex objects that consist of quarks and gluons, as hadrons and nuclei, is not possible yet. A great effort has been made on the theoretical side to develop frameworks to predict and explain the observable part of QCD, as for example lattice-QCD. On the experimental side modern facilities have been constructed and designed to study the interaction among hadrons and to discover new states of matter. In this thesis the main interest is to focus on baryon-baryon interaction in Pb–Pb collisions at the Large Hadron Collider (LHC).

A Large Ion Collider Experiment (ALICE) at the LHC is mainly designed for the investigation of the quark-gluon plasma (QGP). The QGP is a deconfined phase of quarks and gluons. The hot and dense system created in a central nucleus–nucleus collision at LHC energies decays into several thousands of hadrons. In particular, high abundance of strange particles opens the possibility of forming hypernuclei. Hypernuclei are nuclei containing a strange baryon instead of a nucleon, the lightest discovered is the hypertriton consisting of a proton, neutron, and  $\Lambda$ . Other exotic forms of matter such as dibaryons are predicted and their properties calculated, but up to now none was found. They are expected to decay weakly. Confirming the existence of such states can provide a benchmark to theoretical models. One example of these hypothetical dibaryons is the  $(\Xi^0 p)$  dibaryon whose properties are derived in [1]. ALICE is well suited for the search of dibaryons. With the Time-Projection Chamber (TPC), charged particles can be tracked and identified via energy loss. Therefore the charged daughters of dibaryons can be tracked and identified and an invariant mass distribution can be built to identify a signal or, in the absence of a signal, to set an upper limit to their production yield.

On the theory side, yields of light hadrons, (hyper-)nuclei, and dibaryons can be estimated using thermal models. For these models the chemical freeze-out temperature  $T_{ch}$ , the baryo-chemical potential  $\mu_b$  and the volume are the only parameters. The parameters are extracted from fits to hadron yields. Using the hadronization model as described in [5], a yield  $\frac{dN}{dy} = 4.13 \cdot 10^{-3}$  for the  $(\Xi^0 p)$  dibaryon in central Pb–Pb collisions at a center-of-mass energy  $\sqrt{s_{NN}} = 2.76$  TeV is obtained.

The subject of this thesis is the search for the  $(\Xi^0 p)$  dibaryon in central Pb–Pb collisions at a center-of-mass energy  $\sqrt{s_{NN}} = 2.76$  TeV. The thesis is organized in five chapters. Chapter 2 explains the properties of the strange dibaryons and the thermal model to describe their production yield. Chapter 3 contains a brief description of the LHC and of the ALICE apparatus. Chapter 4 presents the analysis performed on Pb–Pb collision data and on a Monte Carlo simulation. The last section draws conclusions and presents an outlook for this study.



---

## 2 Dibaryons

---

The interaction among hadrons is of interest, since the knowledge about it is limited. One way to get further insight into the interaction among baryons is to investigate bound systems. One rare probe for such bound systems are the hypernuclei, which consists of at least one nucleon and at least one baryon with strangeness. Assuming a given binding energy, models can be used to calculate the lifetimes and the decay branching ratios of these systems. The binding energy of the system gives the possibility to calculate with model assumptions the strength and form of the interaction. Dibaryons are systems of two (anti-)baryons. The only known stable dibaryon is the deuteron. It consists of a proton and a neutron. Its mass is  $1.876 \text{ GeV}/c^2$  and its binding energy is  $2.23 \text{ MeV}/c^2$  [6]. The  $(\Xi^0 p)$  dibaryon [1], subject of this work, is assumed to have a decay topology similar to the one of the charged multistrange baryons  $\Xi$  and  $\Omega$  already measured with the ALICE apparatus [2–4].

---

### 2.1 Calculating dibaryon properties

---

Baryons consist of three quarks and are colorless. They interact among each other via the nuclear force. This force can be interpreted as a leftover of the strong force and is described with the exchange of mesons and contact interaction. The resulting potential is attractive, therefore baryons can be bound in nuclei. Deriving the interaction from first principles of the quantum chromodynamics (QCD), the theory of strong interaction, is not possible. In the case of dibaryons several models are used to define the baryon–baryon potential for predictions and calculations, for example model based on SU(3) symmetry or the Nijmegen soft-core model [7]. Several exotic forms of bound quarks and bound baryons have been proposed. In [8, 9] for example, an extended mean field theory is used to predict and calculate properties of bound states containing combinations of p, n,  $\Lambda$ ,  $\Xi^0$  and  $\Xi^-$ . In this approach the baryons remain as baryons, so it is possible for them to occupy the same shell-model state. The binding energy is then limited by the depth of the well and is of the order of 10 MeV. Therefore these objects are stable against strong decays, but decay weakly.

In [1], using SU(3) symmetric contact interactions, the lifetimes and decay channels are calculated. With the SU(3) interactions the weak decay of the octet hyperons can be described. For the nonmesonic decay also the pion and kaon exchange are included. With binding energies of a few MeV, the decay lengths  $c\tau$  of the dibaryons are calculated to be between 1 and 5 cm. The corresponding decay channels with their branching ratios are shown in Figure 2.1. To measure the predicted dibaryons we are interested in decay channels with only charged particles in the final state<sup>1</sup>, since with the TPC only charged tracks can be detected. These decay channels are represented with a solid line.

#### The $(\Xi^0 p)$ dibaryon

For the  $(\Xi^0 p)$  dibaryon the main decay channel for more than 2 MeV binding energy is into a  $\Lambda$  and a proton with a predicted branching ratio between 45 to 65%, right upper panel of Figure 2.1. This decay channel has only charged particles in the final state, since the  $\Lambda$  decays mainly into p and  $\pi^-$ . The decay chain is then

$$(\Xi^0 p) \rightarrow \Lambda + p \rightarrow p + \pi^- + p. \quad (2.1)$$

The branching ratio for the decay of the  $\Lambda$  into p and  $\pi^-$  is about 64% [6], resulting in a total branching ratio for the  $(\Xi^0 p)$  dibaryon to decay into two protons and a  $\pi^-$  between 28 and 42%. For the following

---

<sup>1</sup> Only charged particles in the final states means that after the decay or decay chain the particles are stable within the detector and are carrying a charge.



$V$  is the volume of the fireball,  $g_i$  the spin degeneracy,  $E_i = \sqrt{p^2 + m_i^2}$  is the total energy,  $T_{ch}$  the chemical freeze-out temperature and  $\mu_i$  the baryo-chemical potential. The chemical potential  $\mu_i$  ensures that baryon number, isospin, strangeness, and charm are, on average, conserved

$$\mu_i = \mu_b B_i + \mu_{I_3} I_{3i} + \mu_s S_i + \mu_c C_i. \quad (2.4)$$

With the density

$$n_i = -\frac{T}{V} \frac{\partial \ln Z_i}{\partial \mu} = \frac{\hbar^3 g_i}{2\pi^2} \int_0^\infty \frac{p^2 dp}{e^{(E_i - \mu_i)/T_{ch}} \pm 1} \quad (2.5)$$

the conservation laws require that in total the strangeness and charm are zero and the baryon number and the third component of the isospin match the participating nucleons:

$$\begin{aligned} V \sum_i n_i B_i &= N_B, \\ V \sum_i n_i I_{3i} &= I_3^{tot}, \\ V \sum_i n_i S_i &= 0, \\ V \sum_i n_i C_i &= 0, \end{aligned}$$

Fitting ALICE data, obtained in Pb–Pb collisions at a center-of-mass energy  $\sqrt{s_{NN}} = 2.76$  TeV, the values for the volume  $V$  and the temperature  $T_{ch}$  are  $V = 5300 \text{ fm}^3$  and  $T_{ch} = 156 \text{ MeV}$  [11], which is a bit smaller than the temperature at RHIC. The baryo-chemical potential  $\mu_b$  is fixed to 1 MeV. Using the parameters obtained in the fit and extrapolating the model to other particle masses, the yield at the chemical freeze-out can be calculated (Figure 2.2). With this model the predicted yield  $dN/dy$  of the  $(\Xi^0 p)$  dibaryon for 0 to 10% centrality is  $4.13 \times 10^{-3}$  [11]. This yield is about 5,000 times lower than the yield of the  $\Lambda$ .

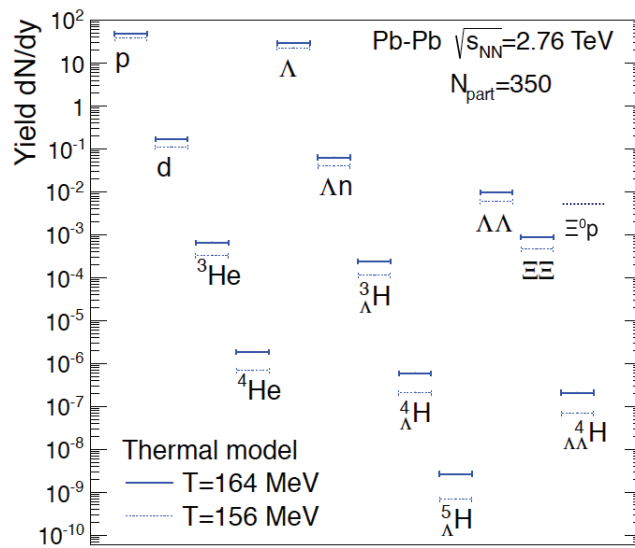


**Figure 2.2:** Production yields  $dN/dz$  from the thermal model for central Pb–Pb collisions.

---

## 2.3 Search for dibaryons

---

In the search for rare state matter, the hypertriton, consisting of a proton, a neutron and a  $\Lambda$ , was the first hypernucleus to be discovered in the year 1952 by Danysz and Pniewski [12]. The ALICE Collaboration has measured the hypertriton at the LHC, too [13], too. On the other hand, in the experimental search for dibaryons, already performed at AGS, SPS and RHIC, despite the effort, no conclusive signal was observed [14]. The most prominent dibaryon is the H-dibaryon (dilambda) proposed by Jaffe [15] in 1977. This state contains of each u, d and s quark two. A recent experimental search for this dibaryon in the decay channel  $H^0 \rightarrow \Lambda + p + \pi^-$  was performed by the ALICE Collaboration [16] and also the STAR Collaboration at RHIC searches for the H-dibaryon [17].

Another candidate is the  $\Lambda n$ , which has the lowest mass of the dibaryons containing strangeness. For this dibaryon the HypHI experiment at GSI observes an enhancement, which is connected to a possible resonance. In [18] no signal in the the decay chain  $\Lambda n \rightarrow \bar{d} + \pi^+$  was observed and an upper limit on the production yield for a bound system was given.

Since in nucleus–nucleus collisions the production of (multi-)strange baryons is abundant compared to pp collisions, the experimental search is concentrated in those collision systems. At the AGS two experiments were looking for the H-dibaryon with tracking and particle identification detectors. Also STAR at RHIC looks for strange dibaryons. With ALICE the search for dibaryons with strangeness continues.

---

### 3 The Experiment

---

A Large Ion Collider Experiment (ALICE) is one of the four large experiments at the Large Hadron Collider (LHC) at CERN in Geneva, Switzerland (see Figure 3.1). ALICE is mainly designed to study the quark-gluon plasma (QGP) in Pb-Pb interactions. In this collision system ALICE is extracting information about how the QGP is created, expands, cools down and turns back to hadrons. As a reference for Pb-Pb and for genuine studies, proton-proton (pp) collisions are also analyzed. Furthermore, ALICE studies cold matter effects in p-Pb and Pb-p interactions.

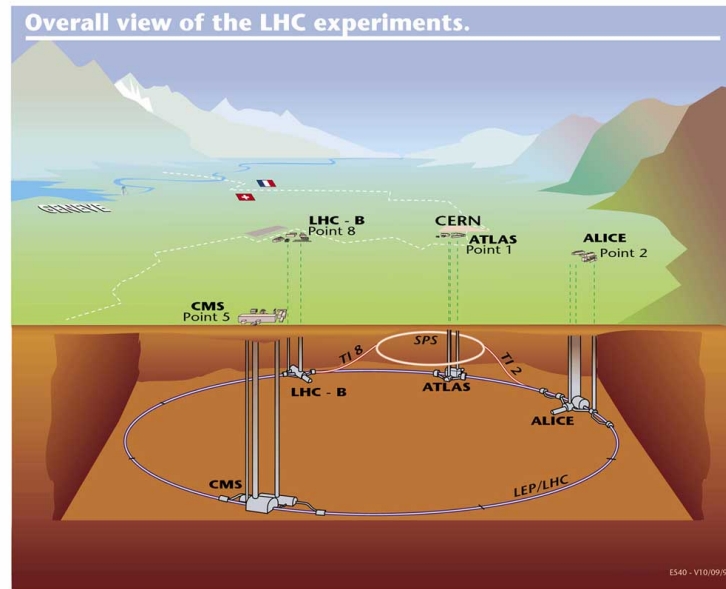


**Figure 3.1:** The LHC with its four large experiments, ALICE, CMS, LHC-b and ATLAS, at the border between Switzerland and France (taken from [19]).

---

#### 3.1 The Large Hadron Collider

---

The LHC project was first proposed in 1984 [20]. It is currently the most powerful accelerator which can collide hadron and nuclei beams, in particular protons and lead ions, at a designed center-of-mass energy  $\sqrt{s} = 14$  TeV for proton beams and at a center-of-mass energy per nucleon pair  $\sqrt{s_{NN}} = 5.5$  TeV for lead beams. So far, the LHC has ran at a center-of-mass energy  $\sqrt{s} = 0.9, 2.76, 7$  and 8 TeV for proton-proton, at a center-of-mass energy per nucleon pair  $\sqrt{s_{NN}} = 2.76$  TeV for Pb-Pb and at a center-of-mass energy per nucleon pair  $\sqrt{s_{NN}} = 5.02$  TeV for p-Pb and Pb-p. The accelerator tunnel is about 26.7 km long and lies between 50 and 175 m below the surface. The beam-line has 1232 dipole and 392 quadrupole superconducting magnets. The magnets operate at a temperature of 1.9 K, the other parts are cooled down to 4.5 K. The collider has four run modes: pp, Pb-Pb, p-Pb and Pb-p collisions. To obtain the proton beams, hydrogen atoms are stripped off their electrons. Then they are accelerated in a linear accelerator (LINAC2), afterwards injected into the PS-Booster and into the Proton-Synchrotron (PS) (see Figure 3.2). They are further accelerated in the Super-Proton Synchrotron (SPS) up to 450 GeV and finally injected into the LHC, where the protons need about 20 minutes to reach the maximum energy. Lead ( $^{208}\text{Pb}$ ) ions are provided by vaporized lead and are then accelerated by LINAC3 and the low energy ion ring (LEIR) before they are injected into the PS and then take the same path as the protons. The lead beam has 592 bunches with  $7 \cdot 10^7$  ions per bunch and the maximal reached luminosity is  $10^{27} \text{ cm}^{-2}\text{s}^{-1}$ .

Besides ALICE there are three other large experiments LHC-b, ATLAS and CMS at the LHC. The first one searches mainly for Charge-Parity violation in B-meson decays. The other two were designed to search for the Higgs boson, which was discovered in 2012 [21] [22], and physics beyond the standard model like supersymmetry. More details can be found in references [23], [24], [25].

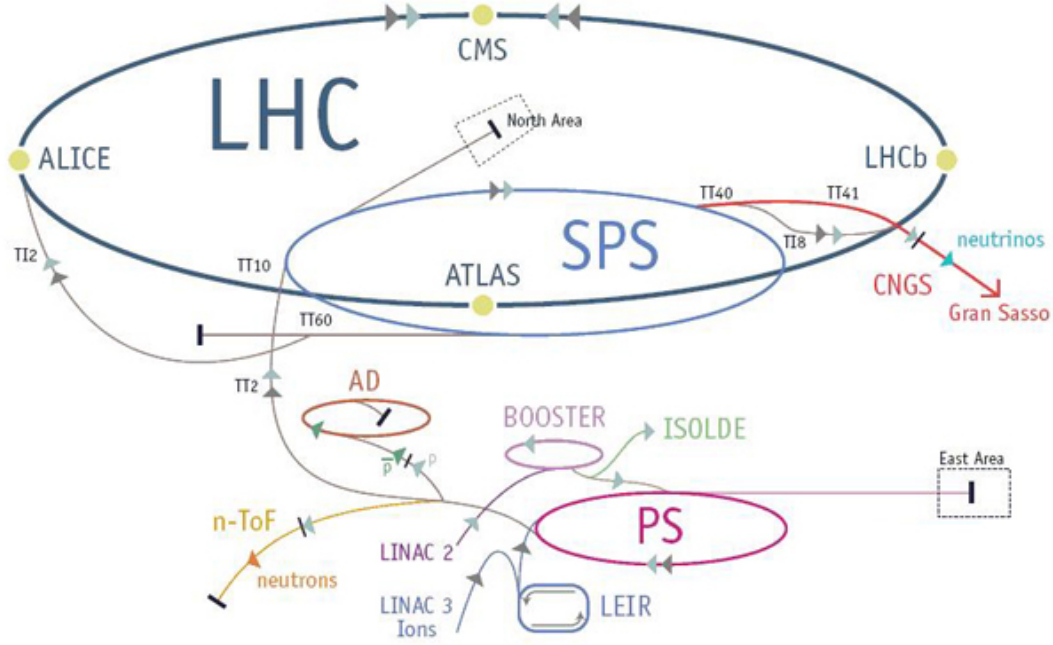


**Figure 3.2:** Schematic picture of the accelerator system at CERN with their connections between each other. Shown are the Large Hadron Collider (LHC), the Super Proton Synchrotron (SPS), the Proton Synchrotron (PS), the Low Energy Ion Ring (LEIR), the LINAC LINEar ACcelerator (LINAC) (taken from [26]).

### 3.2 The ALICE apparatus

The ALICE apparatus is 26 m long and 16 m high and wide. An overview of the detector with the global coordinate system is shown in Figure 3.3. It has a central barrel and forward detectors. The central barrel includes the inner tracking system (ITS), the time projection chamber (TPC) and the transition radiation detector (TRD) as tracking systems. In the central barrel also the time of flight (TOF) detector, which enhances for example the discrimination power between  $\pi/K$  and  $K/p$ , is placed. To further distinguish between particles the high momentum particle identification detector (HMPID) for the momentum region of 3 up to 5 GeV/c is installed. Two calorimeters, the electromagnetic calorimeter (EMCAL) and the photon spectrometer (PHOS), are also hosted in the central barrel. The calorimeters allow to trigger on high-energy jets and photons and to study these observables. The detectors cover a pseudorapidity<sup>1</sup> of  $|\eta| \leq 0.9$  over the full azimuth, except the two calorimeters and the HMPID. The central barrel is included in the L3-magnet of ALICE, which creates a magnetic field of about 0.5 T.

The forward detectors are a single muon spectrometer arm and two zero degree calorimeters (ZDC) to measure proton and neutrons that do not participate in the ion collision (spectators).

The V0 detector is used to minimize background and to determine the centrality<sup>2</sup> of a collision. The T0 is

<sup>1</sup> Pseudorapidity is defined as  $\eta = -\ln(\tan \frac{\theta}{2})$ , where  $\theta$  is the angle between beam axis and the particle trajectory. It is an approximation of the Lorentz invariant rapidity  $y$  in case of high momentum.

<sup>2</sup> Centrality of a heavy ion collision is a variable related to the impact parameter  $\vec{b}$  with which the two ions collide. The centrality ranges between  $b = 0$  (central collision) and  $b = 2R$  (peripheral), where  $R$  is the nuclear radius.



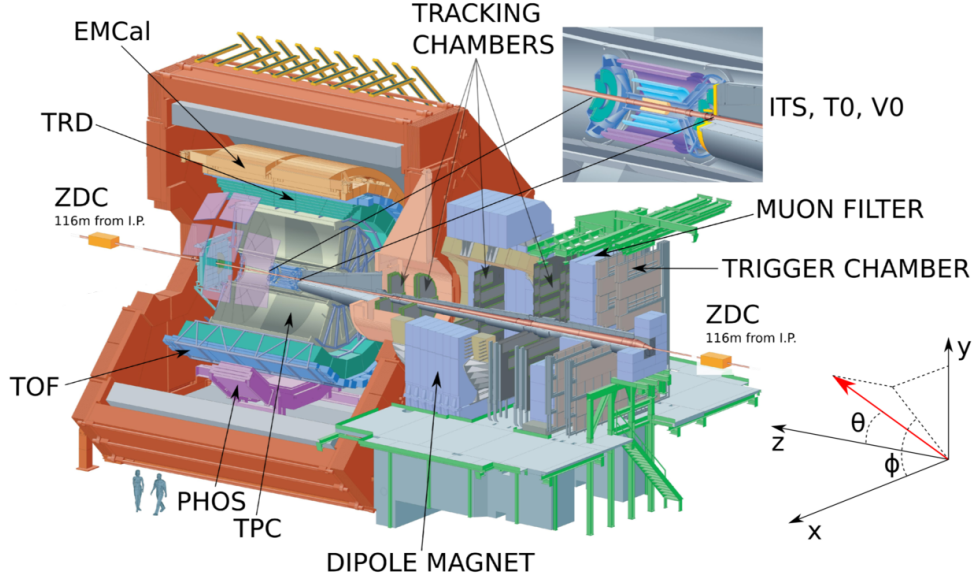


**Figure 3.3:** The ALICE detector system. On the right the global coordinate system with positive  $x$ ,  $y$ ,  $z$  axes is shown together with the spherical coordinates  $r = \sqrt{x^2 + y^2}$ ,  $\phi$ ,  $\theta$ .

used mainly to provide the interaction time.

In the following the ITS and TPC, mainly used in this analysis, are described in more detail. A brief introduction of the V0 follows, since this detector was also used for these studies.

### 3.2.1 The Inner Tracking System

The main tasks of the ITS are the measurement of the primary and secondary vertices and the impact parameter of tracks. This is possible because the ITS provides an excellent spatial resolution of about  $60 \mu\text{m}$  [27]. The ITS is the innermost detector of the central barrel and consists of six cylindrical layers of semiconductor silicon detectors with radii between 4 and 43 cm. Each of the following detector types provides two layers for the ITS starting from the innermost layers: silicon pixel detector (SPD), silicon drift detector (SDD) and double-sided microstrip detector (SSD). All three are tracking detectors, the SDD and SSD provide in addition particle identification via the specific energy loss  $dE/dx$  in the non-relativistic regime down to a transverse momentum  $p_T$  of 0.1 GeV/c (see section 3.2.4).

In semiconductor detectors an incoming charged particle creates hole-electron pairs. With an electric field, the hole and electron are separated and travel to the electrodes. The number of created hole-electron pairs is proportional to the energy loss of the particle.

### 3.2.2 The Time Projection Chamber

The TPC [28] is the main tracking detector. It continues the tracking from the ITS and allows the momentum and the specific energy loss  $dE/dx$  (see section 3.2.4) to be measured down to a transverse momentum  $p_T$  of 0.15 GeV/c. The  $p_T$  resolution of the combined ITS-TPC measurement is about 1% at  $p_T = 1\text{-}2$  GeV/c and about 10% at 100 GeV/c. The  $dE/dx$  resolution of the TPC depends on the multiplicity and the quality of the track, the best achieved resolution is about 5.5%.

The TPC surrounds the ITS, it is about 5.1 m long and has an inner radius of about 0.8 m and an outer radius of 2.5 m. The detector is filled with a mixture of Ne and  $\text{CO}_2$ . The central anode provides a high voltage of 100 kV with about 400 V/cm electrical field strength, resulting in a drift time of about

90  $\mu\text{s}$ . The anode divides the TPC into two parts. At the ends of the tube there are read-out chambers implemented as multiwire proportional chambers with pad read-out. The chambers are segmented in the radial direction into two parts forming inner and outer read-out chambers (IROCs and OROCs). The readout pads are divided azimuthally into 18 segments to match the segmentation of the TOF and TRD detectors. The segmentation leads to different pad densities in the IROCs and OROCs, since the radii are different but the segmentation is the same.

A charged particle, traveling through the gas, ionizes its atoms. Due to the electric field, generated by the central anode, the released electrons travel along the z-axis to the end plates. The drifting electrons of the ionization cannot induce a detectable signal, therefore an amplification is needed. This is achieved with the avalanche effect near the anode wires. The produced positive ions are kept out of the drift field by means of a gating grid.

To reconstruct the track of the particle three coordinates  $r$ ,  $z$  and  $\phi$  are needed. The readout pads give the information of the azimuthal angle and radius of the interaction point. Knowing the drift time and the drift velocity of the electrons in the TPC, the z-coordinate of the interaction point can be determined.

Charged particles are bent by a magnetic field  $B$  provided by L3-magnet to a curve with the radius  $R$ . The radius  $R$  is proportional to the momentum  $p$  and inversely proportional to the charge  $q$ . For high momentum particles the radius goes to infinity. The transverse momentum can be calculated according to

$$p = R \cdot q \cdot B \sin(\alpha), \quad (3.1)$$

where  $\alpha$  is the angle between the momentum  $p$  and the magnetic field  $B$ .

---

### 3.2.3 The V0 detector

---

The V0 detector contributes to trigger minimum-bias events. In Pb–Pb collisions it provides a centrality trigger and can be used offline to estimate the centrality. It can be used for multiplicity measurements and to control the luminosity. The V0 is used to reject background events coming from the interaction between beams and gas in the accelerator.

There are two V0 detectors [29] called V0-A and V0-C, located on both sides of the interaction point. They cover the pseudorapidity ranges  $2.8 \leq \eta \leq 5.1$  (V0-A) and  $-3.7 \leq \eta \leq -1.7$  (V0-C). V0-A is 3.4 m away from the interaction point in the positive z-direction. The V0-C is in front of the muon arm in the negative z-direction, about 0.9 m away from the interaction point.

The V0 detector consist of arrays of scintillator tiles. In scintillators the incoming particles excite the molecules, so that the molecules emit light. The scintillator is transparent to this wavelength. The light can then be bunched and readout with diodes or photomultipliers. The light yield depends on the number of the incoming particles and their energy loss.

---

### 3.2.4 Particle identification by energy loss

---

The ALICE detector employs all known particle identification techniques. The particle identity is determined via energy loss in the TPC and ITS, with the time of flight measured with the TOF, with transition radiation in the TRD and with Cerenkov effect in the HMPID.

In this analysis the energy loss method is used. To identify a particle two pieces of information are needed: the momentum of the particle and the specific energy loss. Both are measured with the TPC. The momentum of the particle can be measured with the tracking detectors as described before.

When a charged particle travels through a medium, it interacts mainly with the electrons of the atoms. The particle loses energy by ionizing or exciting the atoms. The energy loss is specific for each mass and charge. Bethe [30] derived a formula to describe the energy loss in first order

$$\frac{dE}{dx} = -\frac{4\pi}{m_e c^2} \frac{n z^2}{\beta^2} \left( \frac{e^2}{4\pi\epsilon_0} \right)^2 \left( \log \frac{2m_e c^2 \beta^2}{I(1-\beta^2)} - \beta^2 \right), \quad (3.2)$$

with  $E$  being the energy of the particle,  $x$  the traveled distance,  $m_e$  the electron rest mass,  $e$  the elementary charge,  $n$  the electron density,  $z \cdot e$  the charge of the incoming particle,  $\epsilon_0$  the vacuum permeability,  $I$  the mean excitation energy and  $\beta$  the velocity divided by the speed of light  $v/c$ .

Higher order corrections such as Bloch correction, shell correction and density correction improve the accuracy of the formula. The density correction takes the polarization of the electric field into account, thus reducing long range contributions and it is important for high energy particles. The shell correction is important at low energy where capture processes have to be taken into account.

In the experiment, at low  $p_T$  pions, kaons and up to light nuclei can be separated from each other with this method. A performance plot of the TPC with the specific energy loss  $dE/dx$  versus rigidity<sup>3</sup> is shown in Figure 3.4. The theoretical predicted values are highlighted as dashed lines. At higher momentum, the different lines of the specific energy loss start to overlap and the distinction between the different particle species is no longer possible. Then the TOF, HMPID or TRD can be used in addition.

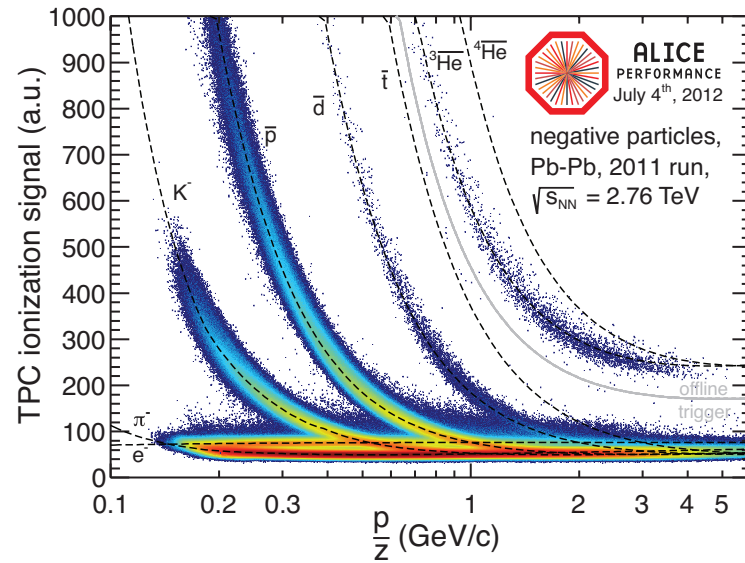


**Figure 3.4:** Specific energy loss  $dE/dx$  measured with the TPC versus rigidity  $\frac{p}{z}$ , here only for negative charged particles in Pb–Pb collisions at a center-of-mass energy  $\sqrt{s_{NN}} = 2.76$  TeV, is shown. The dotted lines correspond to the theoretical predictions for the different particle species. Only events with at least one  ${}^3\text{He}$  candidate are used.

### 3.2.5 Particle identification by weak decay topology

Neutral particles, which decay weakly into two charged daughters, can be detected exploiting their decay topology. A schematic picture of such a decay is shown in Figure 3.5. These decays have a V-shape, since the daughters are boosted in the momentum direction of the mother, therefore these particles are called  $V^0$ s. The opposite charged daughters traveling through the magnetic field in ALICE are bent away from each other.

In ALICE this approach is used to reconstruct for example  $\gamma$  (via conversion),  $K_S^0$ ,  $\pi^0$  and  $\Lambda$ . First opposite charged tracks are combined, then to increase the significance topological selection criteria are applied on the candidates. In Figure 3.5 some of the topological variables used to reconstruct the decay are shown. To reduce the contamination from primary particles, the impact parameter, distance of closest approach to the primary vertex, of the daughters can be used. In addition, the distance of closest approach between the daughter tracks should be small, since they come from the same secondary vertex. Further

<sup>3</sup> The rigidity is the momentum  $p$  divided by the charge  $z$  of the particle.

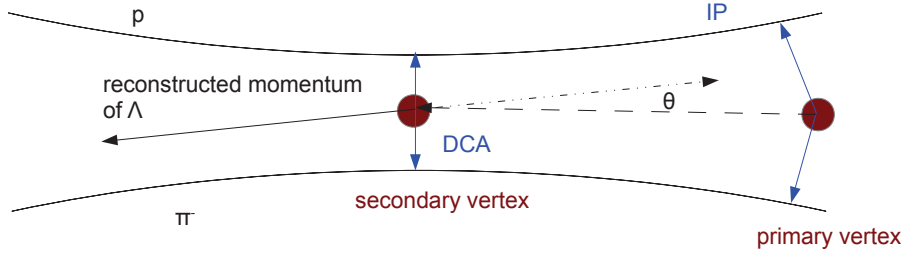


**Figure 3.5:** Schematic picture of the  $\Lambda$  decay:  $\Lambda$  decays into a proton and a  $\pi^-$  at the secondary vertex. The distance of closest approach (DCA) between the negative and positive daughters, the pointing angle  $\theta$  and the impact parameter (IP) of the two daughters are shown.

selection criteria are applied on the reconstructed  $V^0$ , such as the cosine of pointing angle and the fiducial volume for the secondary vertex. The pointing angle is the angle between the reconstructed momentum of the  $V^0$  and the line which connects the secondary vertex with a point. With this variable the  $V^0$  can be constrained to come from this point. For primary  $V^0$ s the point is the primary vertex. The fiducial volume is the volume in which the reconstructed secondary vertex should be.

Particles decaying into a weakly decaying neutral particle and a charged one, called cascades, can be reconstructed using a similar method, Figure 3.6. As described above the  $V^0$  candidates are reconstructed and then they are selected if the invariant mass, built with the  $V^0$  daughters, is within a certain window around the PDG mass value of the mother. Then afterwards the candidate is combined with a third track, the so called bachelor. The bachelor is identified according to the decay chain, for the investigated dibaryon it is identified as a proton. Selection criteria on topological variables are used to increase the significance. The impact parameter of the cascade daughter tracks, the  $V^0$  and the bachelor tracks, can be used to reject primary candidates, as primary tracks should have a small impact parameter. The distance of closest approach between the two daughters can be evaluated, as daughters of the same mother should be close together in space. The fiducial volume can be used for the cascade vertex, if the decay length is known. As we have two reconstructed particles, the decaying daughter and mother, we can use both cosine of pointing angles. The first one is the cosine of pointing angle of the  $V^0$ , which can be calculated with respect to the secondary vertex, in order to reject primary  $V^0$ s. The second one is the cosine of pointing angle of the cascade and it is calculated with respect to the primary vertex. This strategy based on the decay topology is used to reconstruct the  $(\Xi^0 p)$  dibaryon, which decays into a  $\Lambda$  and a positive charged proton. This strategy is also used in the analysis of the already reconstructed particles  $\Xi^-$  and  $\Omega^-$  which decay into a  $\Lambda$  and into a negative charged bachelor ( $\pi^-$  and respectively  $K^-$ ) instead of a positive charged bachelor.

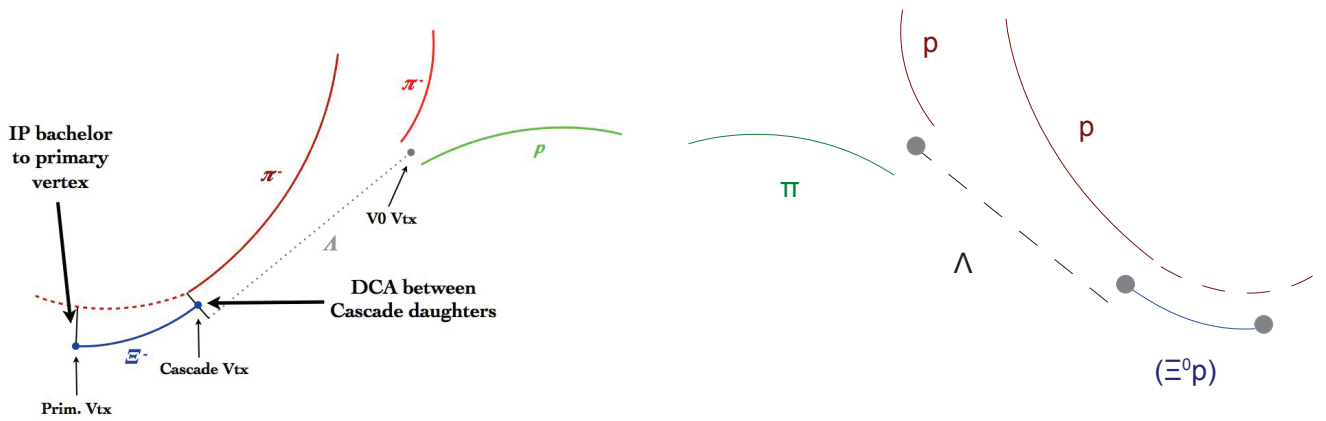


**Figure 3.6:** Left: schematic picture of the  $\Xi^-$  decay:  $\Xi^-$  decays into a  $\pi^-$  and a neutral  $\Lambda$  at the secondary vertex. The distance of closest approach (DCA) between the bachelor and  $\Lambda$  daughter, and the impact parameter (IP) of the bachelor track are shown. Right: schematic picture of the  $(\Xi^0 p)$  dibaryon decay: It decays into a positive charged proton, instead of a pion and a neutral  $\Lambda$ . The same variables can be used to describe the decay topology.



---

## 4 Analysis

---

This chapter presents the analysis and the results obtained in this work. In the first section the selection criteria for the events and tracks are described, followed by the description of the selection criteria for the dibaryon reconstruction. a study on a Monte Carlo simulation to optimize the selection criteria for the dibaryon reconstruction is presented and the reconstruction efficiency is computed. Finally the invariant mass distribution is shown and an upper limit to the production yield of the ( $\Xi^0$ p) dibaryon is estimated. The analysis is done with AliRoot [31], the official framework, based on ROOT [32], developed by the ALICE Collaboration for simulation, reconstruction and data analysis.

---

### 4.0.6 Event and Track selection

---

The used data and Monte Carlo sample and the events selection criteria to remove background events are described here. Subsequently the track selection criteria to use only tracks with good quality are defined.

#### Data sample and event selection

The data used for this analysis were taken in 2010 during the first Pb–Pb run with a center-of-mass energy per nucleon pair of  $\sqrt{s_{NN}} = 2.76$  TeV. After applying the selection criteria (Table 4.1) on the events, about 13.5 million events in the centrality range from 0 to 80% are analyzed. The event selection criteria reject background events, for example coming from beam-gas interactions. Only events with a primary vertex position within 10 cm from the center of the detector along the beam line are selected to ensure a good rapidity coverage and uniformity for the particle reconstruction efficiency in the ITS and TPC tracking volume.

For the Monte Carlo study a local production anchored to these data is used. In this production hypertriton,  $\Lambda_n$ , H-dibaryon,  $\text{Ann}$ , the ( $\Xi^0$ p) and the corresponding antiparticles are added on top of minimum bias HIJING events, using AliGenBox. Ten of each particle type are injected flat in transverse momentum  $p_T$  from 0 to 10 GeV/c and rapidity  $y$  from -1 to +1. The centrality of the events is from 0 to 5% and about 22 thousand events are generated. A Monte Carlo production anchored to the data taken in 2011 in Pb–Pb collisions with a center-of-mass energy per nucleon pair of  $\sqrt{s_{NN}} = 2.76$  TeV is available. In this production the weakly decaying ( $\Xi^0$ p) and  $\text{Ann}$  and additionally the nuclei deuteron, triton, helium-3, and helium-4 together with their antiparticles are injected. The injection pattern is similar to the one described for the local production. About 300 thousand events in the centrality range from 0 to 80% are produced.

#### Track selection

In these selected events tracks have to fulfill quality conditions in order to provide tracks with good quality. They are the following:

**Table 4.1:** Event selection criteria

Selection criteria	
trigger	minimum bias
centrality	0-80%
vertex position in z	$\pm 10$ cm

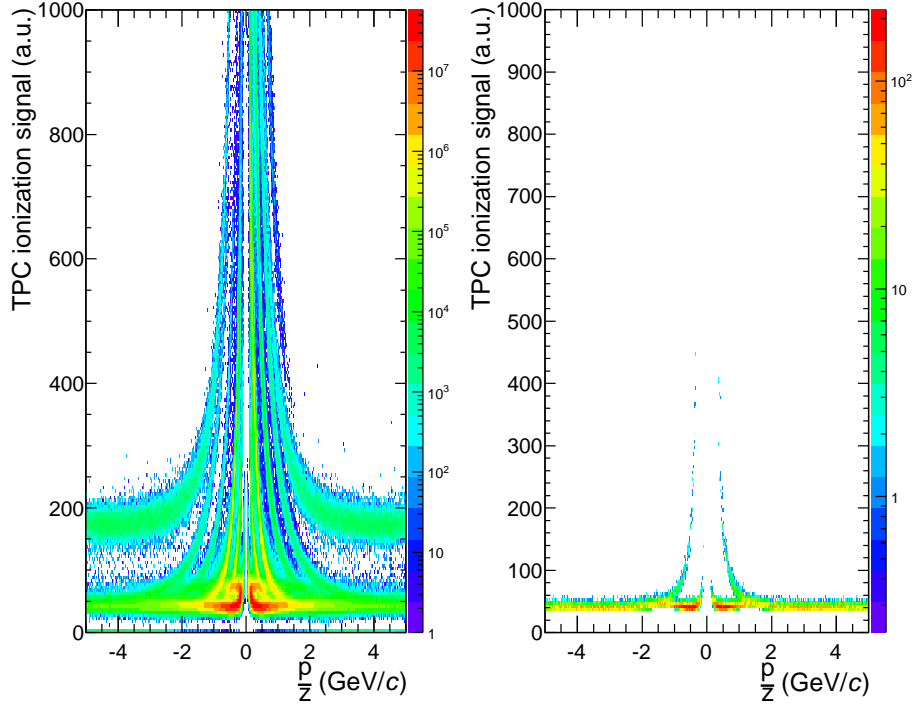


**Figure 4.1:** In Monte Carlo reconstructed ionization signal of the TPC for all particles (left panel) and for the reconstructed tracks which are daughters of  $(\Xi^0 p)$  dibaryons (right panel). The bands of the particles can be identified, going from 0 to 5 rigidity, as positron,  $\pi^+$ ,  $K^+$ , proton, deuteron, helium-3, and going in the other directions as their (anti-)particles.

- The number of TPC clusters per track is set to be greater than 70 and the  $\chi^2$  per cluster is set to be less than five. In addition the TPC refit is required. These three criteria secure an accurate tracking, and a good resolution of the momentum and the energy loss measurement.
- The pseudorapidity  $\eta$  is restricted to the interval from  $-0.8$  to  $+0.8$ . This secures that the tracks are within the acceptance window.

#### 4.1 Reconstruction strategy for the dibaryon

As already mentioned in section 3.2.5 the decay topology of this dibaryon is very similar to the one of the charged cascades  $\Xi$  and  $\Omega$  (Figure 3.6) therefore a similar approach is used. The code used for cascade reconstruction (AliCascadeVertexer) cannot be used since this algorithm combines a  $V^0$ , assumed to be a  $\Lambda$ , with a negative charged bachelor track and in the case of the  $(\Xi^0 p)$  dibaryon the  $\Lambda$  has to be combined with a positive charged bachelor track.

The strategy to reconstruct the dibaryon is first to build and select the  $\Lambda$  candidate using the PID information from the TPC on the two daughter tracks. The candidate is then combined with the bachelor, identified as proton, to form a  $(\Xi^0 p)$  dibaryon candidate. The dibaryon candidates will then be selected with topological and kinematical criteria.

The  $V^0$  particles in ALICE, two algorithms exist, one that operates during the event reconstruction and one after track reconstruction. They are called the online and offline (AliV0Vertexer)  $V^0$  finder and use the logic presented in Section 3.2.5, with different selection criteria. To reconstruct the  $\Lambda$ , the offline  $V^0$  finder was chosen, because it has a higher efficiency to reconstruct secondary  $V^0$  particles compared to the online  $V^0$  finder. The used by the offline  $V^0$  finder are listed in Table 4.2. The  $V^0$  candidates found by the



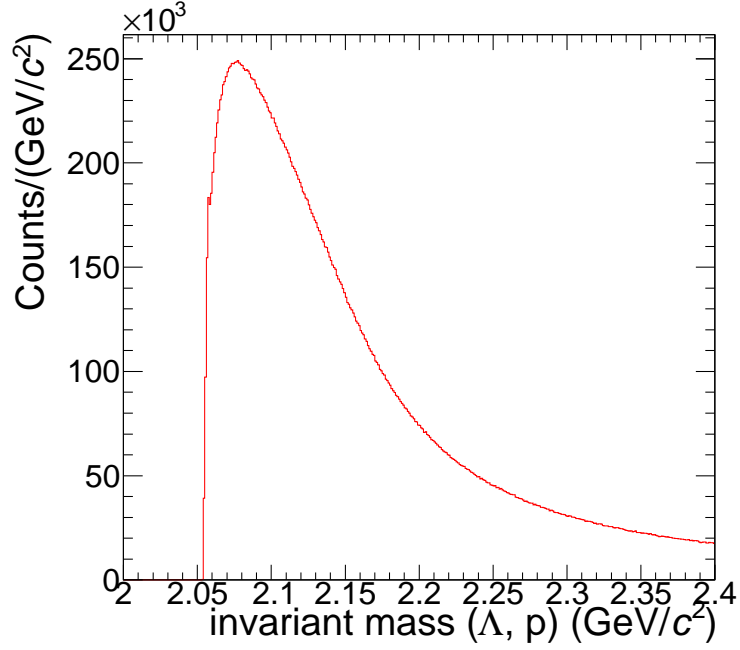


**Figure 4.2:** Invariant mass distribution of  $\Lambda$  and protons combined with the invariant mass distribution of their antiparticles obtained with loose reconstruction criteria using the Pb–Pb collision data at a center-of-mass energy  $\sqrt{s_{NN}} = 2.76$  TeV in the centrality range from 0 to 80%.

**Table 4.2:** Selection criteria and corresponding values used to reconstruct  $V^0$  particles in the offline V0 finder.

Topological variables	Values for Pb–Pb events
Impact parameter in xy for the daughters	$> 0.1$ cm
Distance of closest approach between daughter tracks	$< 1$ cm
Cosine of pointing angle with respect to primary vertex	$> 0.998$
Radius of the fiducial volume in xy	$> 0.9$ cm
	$< 100$ cm

offline finder are selected for this analysis only if both daughter tracks meet the quality track criteria and are identified as a proton and a pion with the TPC, using the energy loss method described in 3.2.4. An example for the resulting energy loss distribution of tracks as a function of the rigidity is shown for data as a performance plot in Figure 3.4 and for the Monte Carlo simulation in Figure 4.1. In the left panel of Figure 4.1 all tracks, traveling through the TPC, are plotted. Going from 0 rigidity towards higher rigidity one sees the positron,  $\pi^+$ ,  $K^+$ , proton, deuteron and helium-3 bands. Going in the other direction the bands of the corresponding antiparticles can be identified. The deuteron and helium-3 band are so clearly visible, because in the Monte Carlo the injected  $\Lambda n$  decays into a deuteron and a  $\pi^-$  and the enhanced hypertriton decays into helium-3 and  $\pi^-$ . In the right panel of the same figure only tracks which are daughters of  $(\Xi^0 p)$  dibaryon shown. Finally,  $\Lambda$  candidates are selected by requiring an invariant mass within a mass-window around the  $\Lambda$ -mass.

Combining the  $\Lambda$  candidate with the bachelor, identified as a proton, the dibaryon candidate is formed and, similarly, combining the antiparticles, the antidibaryon is reconstructed. In the following the particle and the antiparticle are combined together. As for the  $\Lambda$  reconstruction, topological criteria are applied. For example the cosine of pointing angle of the dibaryon with respect to the primary vertex is the most effective criterion in terms of increasing the significance. In addition, two logical criteria are required. The first is that the  $\Lambda$  decays after the dibaryon and the second is that the scalar product of the momenta

**Table 4.3: Reconstruction criteria for the dibaryon**

Selection criteria	loose values
$ M(p, \pi) - m_\Lambda $	$< 15 \text{ MeV}/c^2$
Impact parameter in xy for the $\Lambda$	$> 0.02 \text{ cm}$
Impact parameter in xy of the $p_{\text{Bach}}$	$> 0.02 \text{ cm}$
Distance of closest approach between $\Lambda$ and $p_{\text{Bach}}$	$< 1.5 \text{ cm}$
$\cos(\theta_{pA})$ of $(\Xi^0 p)$ wrt primary vertex	$> 0.97$
$\cos(\theta_{pA})$ of $\Lambda$ wrt $(\Xi^0 p)$ vertex	$> 0.97$

of the  $\Lambda$  and of the  $(\Xi^0 p)$  dibaryon has to be greater than zero. The first one is obvious and the second one can be understood easily, with the argument of momentum conservation. The two daughters, proton and  $\Lambda$ , are boosted in the direction of the dibaryon. Thus, the scalar product is greater than zero.

With this strategy analyzing the data with very loose values for selection criteria, in the following called reconstruction criteria (Table 4.3), one gets an invariant mass distribution in which no signal is observed (Figure 4.2). The invariant mass distribution shoots up and then decreases fast. The reconstruction criteria are very loose in comparison to the selection criteria used for the multi-strange baryon reconstruction, so it is expected not to see the signal. Stronger cuts should be used to reduce the background. A study performed on Monte Carlo events for this purpose is presented in the next paragraph.

---

## 4.2 Monte Carlo simulation study

---

The goal of this study on Monte Carlo simulations is to tighten the selection criteria for the  $(\Xi^0 p)$  dibaryon, which are described in Section 3.2.5, to enhance the significance and consequently to reduce the background in the data. All the useful topological and kinematical variables both for the  $\Lambda$  and the  $(\Xi^0 p)$  dibaryon are analyzed in more detail in the the next section.

The Monte Carlo study starts by building the invariant mass of  $\Lambda$  and proton with the same reconstruction criteria used for data. No clear peak in the invariant mass distribution is visible, Figure 4.3, but a small bump. In Figure 4.3 the reconstructed injected signal in the invariant mass distribution is represented with a red line and it lies at the same position as the bump. The invariant mass distribution of the reconstructed Monte Carlo truth dibaryons has a Gaussian shape with a mean value  $2.248 \text{ GeV}/c^2$ , which is the simulated mass, and the standard deviation  $\sigma$  of the signal is  $9.0 \text{ MeV}/c^2$ . In the following the background and the signal are separated using the Monte Carlo truth information and selected in a  $3 \sigma$ -wide region around the injected mass. For all the topological and kinematical variables listed in Table 4.2 and 4.3 the distribution and their integrated fractions are presented and compared both for the signal (red) and the background (blue).

---

### Selection Criteria for $\Lambda$ -candidate

---

A cut on the impact parameter of the daughter tracks of the  $V^0$  is applied in the offline  $V^0$  finder, as already mentioned. The value is for both tracks  $0.1 \text{ cm}$  as it can be seen in Figure 4.4, where the distributions of the impact parameters of both  $\Lambda$  daughters are shown for the signal (red) and the background (blue) in the first panel for charged pions and in the third for (anti-)protons. It is clear that the distributions for the background are peaked at small values for the impact parameter, because the main contribution is given by primary particles. For the signal the distributions are almost flat being these secondary particles. From

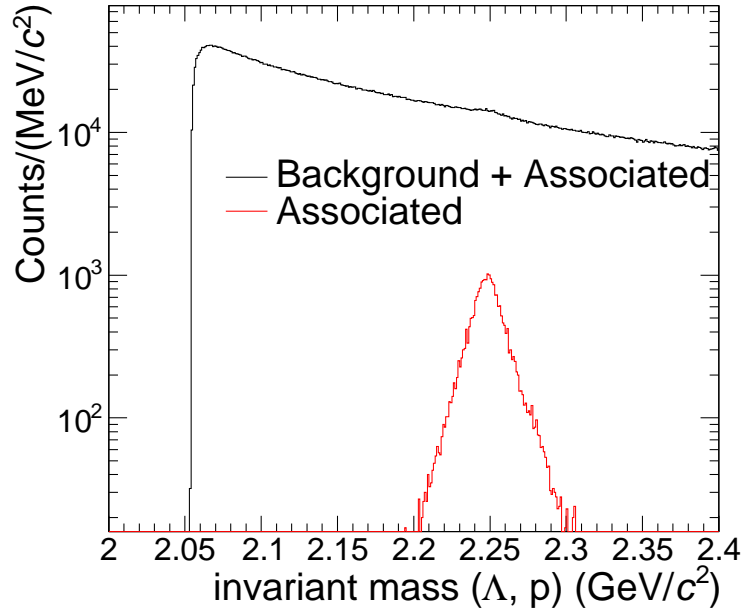


**Figure 4.3:** Invariant mass distribution of  $\Lambda$  and proton and their antiparticles obtained with the local Monte Carlo simulation applying the reconstruction criteria. A small bump can be seen at the injected mass. The red curve represents the reconstructed signal.

the corresponding integrated fractions, shown in the second and fourth panel of Figure 4.4, tighter limits can be set: increasing the lower limit to 1 cm for the pion and to 0.4 cm for the proton. For these limits the background is reduced to about 52% for pions and to about 35% for protons. The signal is reduced to 85% and 80% respectively.

#### $\Lambda$ candidate selection

After the selection of the tracks, the possible  $\Lambda$  daughters are combined. As the two particles, as daughters of the same mother, should come from the same (secondary) vertex, the distance of closest approach between them should be small. The normalized distribution of the distance of closest is shown in Figure 4.5 with the integrated distribution to the right. The distribution of the integrated background in the right panel is almost a linear function of the distance of closest approach and increases faster than the signal. Setting an upper limit down to 0.4 cm results into losing 53% background and 10% signal.

As the  $\Lambda$  has the  $(\Xi^0 p)$  dibaryon as a mother, the  $\Lambda$  should also be a secondary particle, like its daughters. The impact parameter of the  $\Lambda$  is calculated. The distribution in the left panel of Figure 4.6 shows the impact parameter of the  $\Lambda$  candidates. The background is peaked at small values for the impact parameter, since primary  $\Lambda$  are contributing as well, whereas the signal has a much weaker dependence. The impact parameter can be limited to be greater than 0.2 cm. This would remove 56% of the background and keep 81% of the signal.

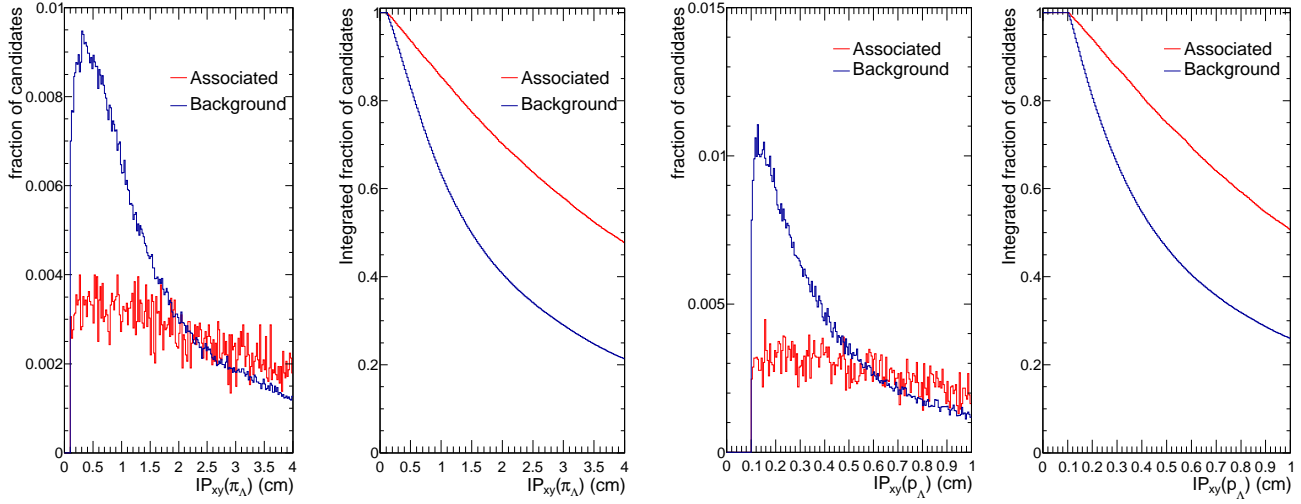


**Figure 4.4:** Impact parameter in xy of charged  $\pi$  (first panel) and (anti-)proton (third panel) originating from a  $V^0$ -candidate. The distributions are normalized to their integral. The integrated distributions as a function of the impact parameter are shown for the charged  $\pi$  (second panel) and the (anti-)proton (fourth panel).

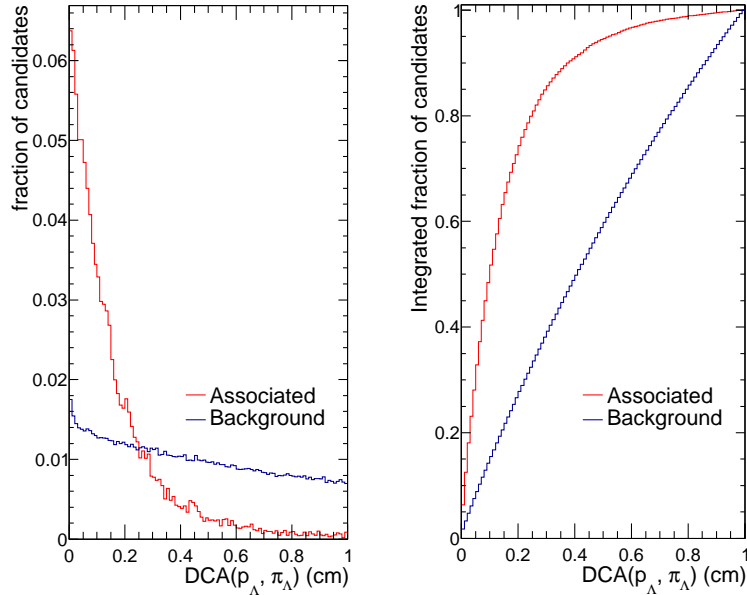


**Figure 4.5:** Normalized distribution of the distance of closest approach between the two  $\Lambda$ -candidate daughters ((anti-)proton and charged  $\pi$ ) (left panel) and its integrated distribution as a function of the distance of closest approach (right panel) are shown.

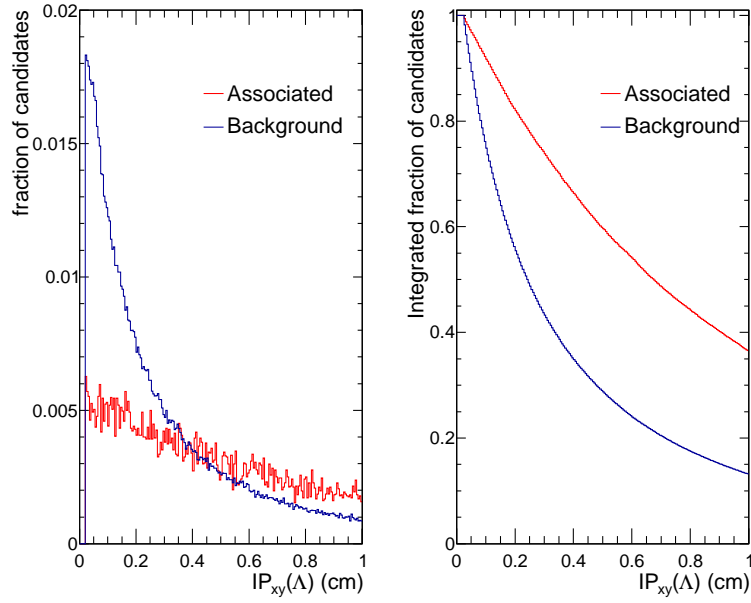


**Figure 4.6:** Normalized distribution of the impact parameter in xy of the  $\Lambda$ -candidates (left panel). The background (blue) shows a peak at small impact parameters, the signal (red) has a weaker dependence. Their integrals as a function of the impact parameter are shown in the right panel.

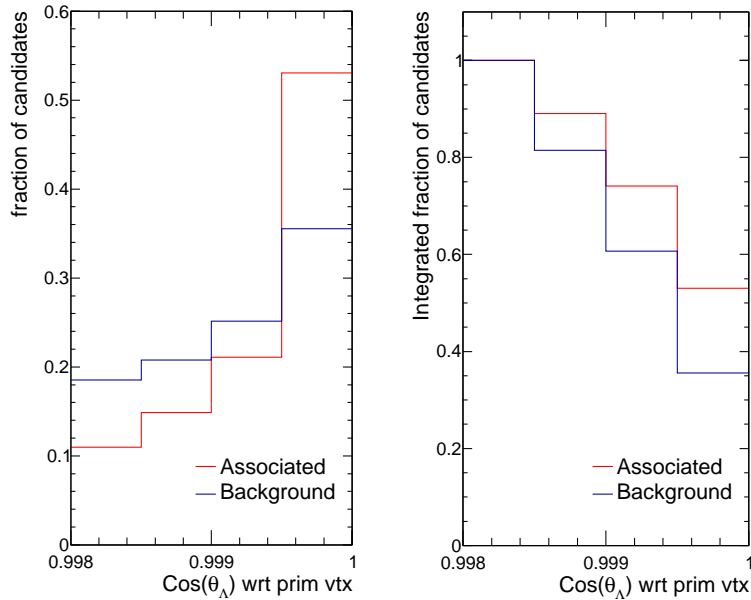


**Figure 4.7:** Normalized distribution of the cosine of pointing angle of the  $\Lambda$  candidate with respect to the primary vertex (left panel) and the integral (right panel) are shown. The distributions of the background (blue) and signal (red) are similar. Their integrals are shown in the right panel.

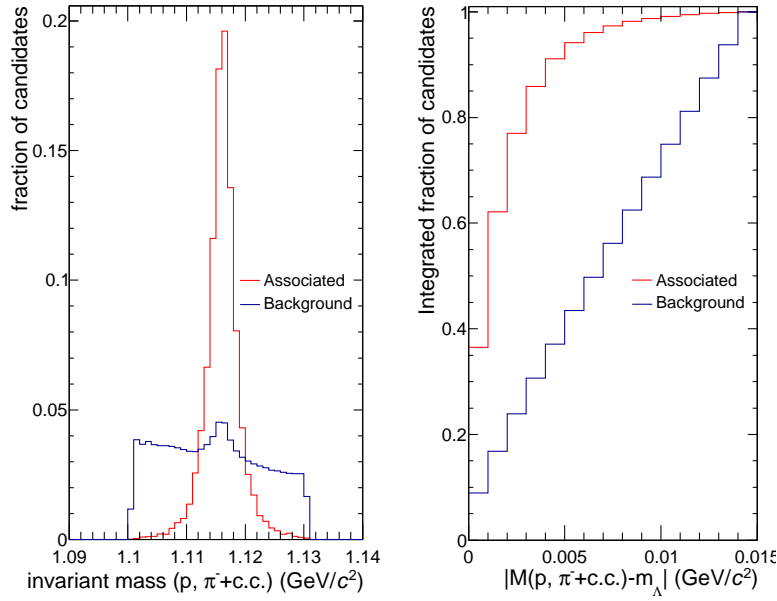


**Figure 4.8:** Normalized invariant mass distribution of  $\pi^-$  and proton, and their antiparticles (left panel) and the integrated absolute difference of invariant mass and the  $\Lambda$  mass  $m_\Lambda$  (right panel) are shown.

The cosine of pointing angle with respect to the primary vertex of the  $\Lambda$  candidate, is already limited to 0.998 on the reconstruction level of the  $V^0$  finder. Its distribution is shown in Figure 4.7. The shape of the distributions for the background and signal are similar, therefore this cut is not changed. However since the  $\Lambda$  which are daughters of the dibaryons should not point back to the primary vertex but to the secondary vertex it can be useful to calculate this variable with respect to the secondary vertex. This will be addressed later.

The dibaryon candidates have been selected requiring the  $\Lambda$  to have a mass in an interval within  $15 \text{ MeV}/c^2$  around the peak. To tighten this criterion means to increase the ratio between true  $\Lambda$ s and combinatorial background. In Figure 4.8 the distribution is shown. For both the background and the signal the  $\Lambda$  peak is visible in the left panel. The peak in the background is due to true  $\Lambda$ s, which come from other decays or are primaries. To identify the  $\Lambda$ s we switch to the absolute difference between the invariant mass of the proton and pion, and the  $\Lambda$ -mass. This is allowed, because the detector resolution is approximately Gaussian and dominates the shape of the peak. This results in the integrated distribution in the right panel. The difference can be restricted further to  $8 \text{ MeV}/c^2$ , removing the background to 55% and keeping 97% of the signal. This interval corresponds to about  $3 \sigma$  region around of the  $\Lambda$ -mass.

---

#### Selection criteria for the $(\Xi^0 p)$ dibaryon candidates

---

After selecting the  $\Lambda$  candidate, the bachelor proton is combined with it, if the requirements described in the following are fulfilled.

Applying the track selection and the PID criteria on the bachelor track, a cut on the impact parameter is applied. In the reconstruction the value was set to 0.01 cm. The distribution of the impact parameter is shown in the left panel of Figure 4.9. In the background distribution a peak at small values

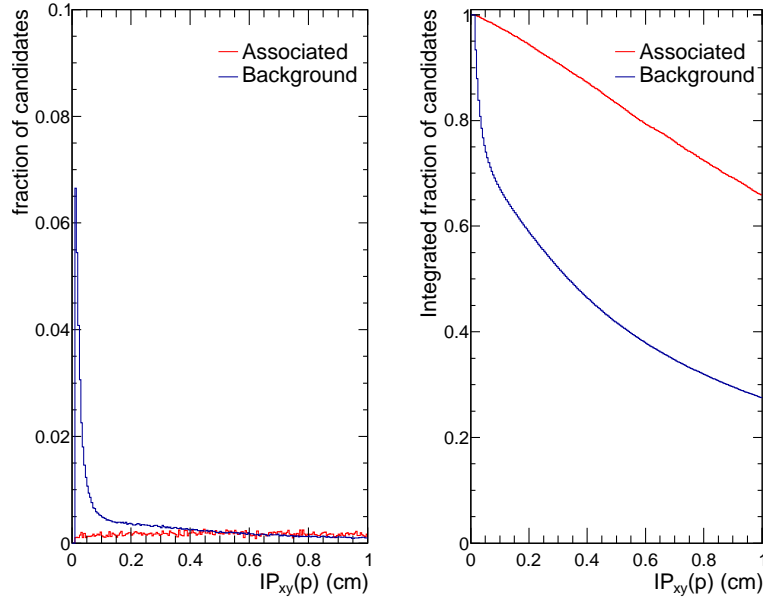


**Figure 4.9:** Normalized distribution of the impact parameter in xy for the bachelor proton is shown in the left panel. A clear peak at small impact parameters in the background distribution (blue) can be seen. The cause are primary particles, which have small impact parameters. The integrated distributions are shown in the right panel.

for the impact parameter is visible, because the main contribution is given by primary particles, as already mentioned. The lower limit should be greater than 0.1 and was set to 0.3 cm. This will remove about 28% of the background and keep 94% of signal.

Like in the algorithm to find the multi-strange cascades, the option to requirement of having hits in the ITS for the bachelor is checked. This option is found to be too strong since the simulated lifetime is about the  $\Lambda$  lifetime  $c\tau \approx 7.89$  cm, which is higher than charged cascade lifetimes (for  $\Xi$ ,  $c\tau \approx 4.91$  cm and for the  $\Omega$   $c\tau \approx 2.461$  cm) which enhances the probability for the bachelor track to have hits in the ITS.

### $(\Xi^0 p)$ dibaryon selection

Following the same logic and order as for the  $\Lambda$  reconstruction, the distance of closest approach between the  $\Lambda$  and proton is evaluated. The distribution is shown in Figure 4.10. It is not limited at 1 cm as it was for the  $\Lambda^1$  daughters, but at 1.5 cm. The integral of the distance of closest approach for the associated<sup>2</sup> dibaryons shows a smooth increase at distances larger than 0.4 cm whereas the background increases faster. The upper limit should be small as 0.4 cm. This will remove about 31% of the background and keep 94% of the signal.

<sup>1</sup> The difference is due to the fact that the offline  $V^0$  finder already requires such a small distance of closest approach. In order to keep most of the signal, the distance of closest approach between  $\Lambda$  and bachelor proton was set to be less than 1.5 cm to ensure no signal is missed.

<sup>2</sup> Associated means that the reconstructed dibaryon corresponds to a Monte Carlo truth dibaryon.

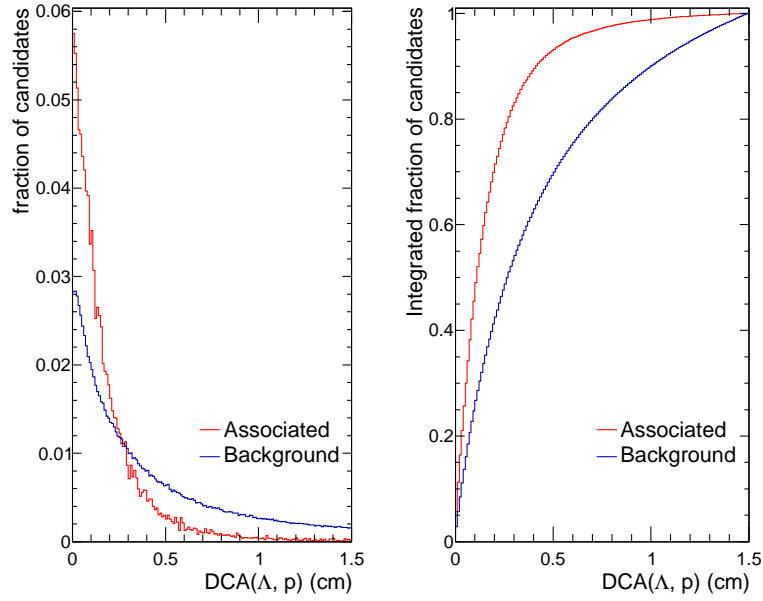


**Figure 4.10:** Normalized distribution of the distance of closest approach between the  $\Lambda$  and the bachelor proton is shown in the left panel. It is peaked for the signal (red) at small distances, whereas for the background (blue) it is smeared out. The integrated distributions are shown in the right panel.

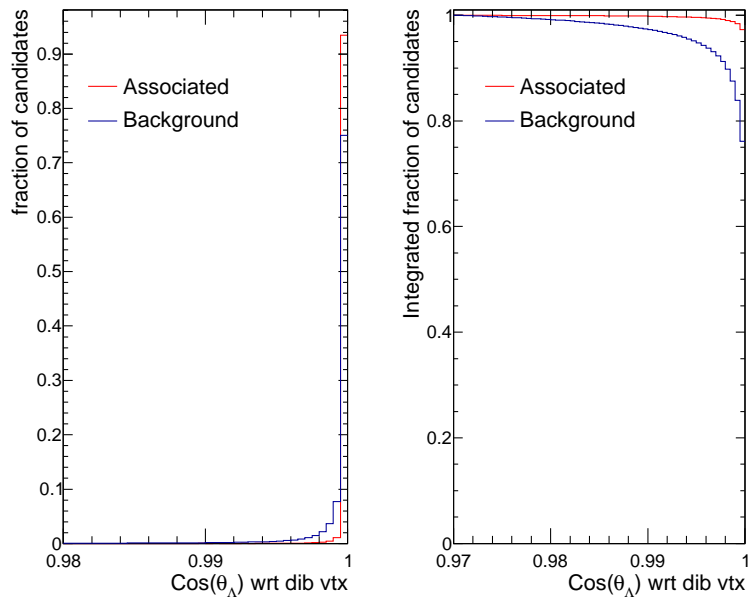


**Figure 4.11:** Normalized distribution of the cosine of pointing angle of the  $\Lambda$  candidate with respect to the dibaryon vertex is shown. The  $\Lambda$  as a daughter of the dibaryon should have a value almost to one, which can be seen.



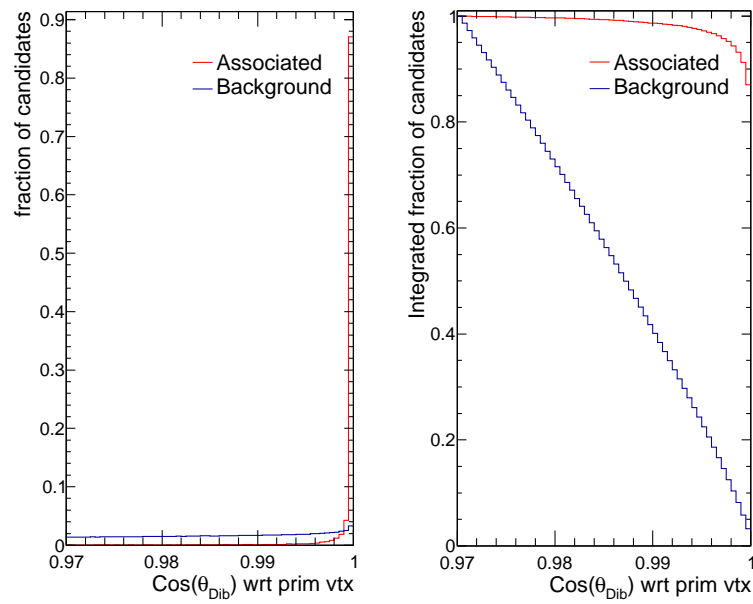


**Figure 4.12:** Normalized distribution of the cosine of pointing angle of the dibaryon with respect to the primary vertex is shown. It is the strongest selection criterion, as only the signal (red) is peaked at one, whereas the background (blue) is flatly distributed.

In the decay topology two cosine of pointing angles can be useful. One is the cosine pointing angle of the  $\Lambda$  with respect to the decay point of the dibaryon and the other one is the cosine of pointing angle of the dibaryon with respect to the primary vertex. For the first variable the distribution is shown in Figure 4.11. As the  $\Lambda$  originates from this vertex it should point back to it, resulting in the peak at one. For the background the peak at one can be explained, too, as the cosine of pointing angle of the  $\Lambda$  with respect to the primary vertex constrains it already (Table 4.2 and combining it with another particle with small impact parameter the angle should not change much. In addition, the distance of closest approach biases the distribution, as the point of closest approach should be near the connecting line of the  $\Lambda$  decay point and the primary vertex. The distribution suggests a lower limit like 0.999, which is almost the same as for the cosine of pointing angle of the  $\Lambda$  with respect to the primary vertex, thus removing almost 30% of the background and keeping 99% of the signal.

The cosine of pointing angle of the  $(\Xi^0 p)$  dibaryon is the strongest criterion in terms of enhancing the significance. The distributions of the cosine of pointing angle of the dibaryon is shown in Figure 4.12. The background is almost equally distributed over the whole range, whereas the signal is almost only in the region above 0.999. Thus, setting the lower limit to this value about 86% of the background is removed and 95% of the signal is kept.

Going back to the cosine of pointing angle of the  $\Lambda$  candidate with respect to the primary vertex after applying all the selection criteria, as mentioned before, no indication is given to change the limit of this criterion.

All the selection criteria may depend on the transverse momentum of the dibaryon, therefore the study was performed also in several interval of transverse momentum and only a weak dependence is observed. The strongest dependence is expected for the four impact parameters (proton,  $\Lambda$ , proton and  $\pi$ ) and the cosine of pointing angles. The strongest dependence is observed for the cosine of pointing angle of the dibaryon to the primary vertex, shown in the left panel of Figure 4.13. The background has still the same shape, but with less transverse momentum the cosine of the angle is less peaked for the signal. This behavior is expected, as the dibaryon is bend due to the magnetic field. For the invariant mass distribution in bins of transverse momentum  $p_T$ , shown in the right panel of Figure 4.13, the shape does not change, except the peak at the small invariant mass is more significant. The significance of the injected signal increases towards higher  $p_T$  as the background is less and the efficiency higher (the particles are injected flat in  $p_T$ ).

---

### 4.3 Results and discussion

---

Tightening the values of the cuts as proposed in the previous paragraph, the invariant mass distribution of  $\Lambda$  and proton and their antiparticles has in Monte Carlo a clear visible peak at the injected mass with almost no background left (Figure 4.14). A second peak is visible at the lower limit of the invariant mass of about  $2.05 \text{ GeV}/c^2$ . This means that the two daughter particles,  $\Lambda$  and bachelor proton, have almost no relative momentum. Since the invariant mass depends on the relative momentum, it is reduced to its lower limit. If these two particles (proton,  $\Lambda$ ) have similar momenta, then the bachelor proton and the proton coming from the  $\Lambda$  decay have similar momenta, too, because the proton carries most of the momentum of the  $\Lambda$ . The added pion momenta broadens the peak. This structure is might be due to track splitting or hit sharing, therefore in Monte Carlo the difference in the azimuthal angle  $\Phi$  and the pseudorapidity  $\eta$  is evaluated. In Figure 4.15, the two dimensional plot is shown in the left panel for the signal in the peak region, and in the right panel the background in the region with an invariant mass below  $2.1 \text{ GeV}/c^2$ . For the background a peak is visible at small angle differences at (0,0), which is a hint for track splitting. As this structure is far away from the expected signal region and not completely understood no cuts are applied to remove the structure, which would additionally lower the efficiency.

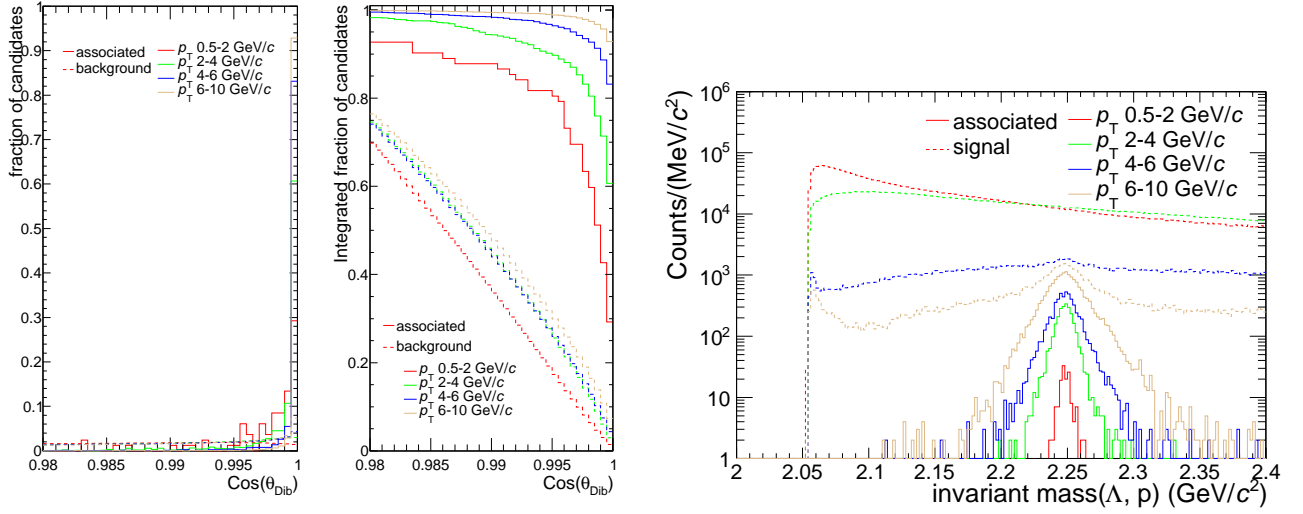


**Figure 4.13:** Normalized distributions of the cosine of pointing angle for the dibaryons and antidibaryon with respect to the primary vertex in different transverse momentum intervals (left panel) are shown. Invariant mass distributions of  $\Lambda$  and proton, and their antiparticles for different transverse momentum intervals (right panel) are shown.

Applying the same tighter criteria to the data obtained in the Pb–Pb run in 2010, the invariant mass distribution of proton and  $\Lambda$  and their antiparticles results into the plot shown in Figure 4.16. No peak in the expected signal region is visible. At the smallest possible invariant mass a spike is visible and might be also due to a stronger effect of track splitting. The track identified as proton is split and used to reconstruct the  $\Lambda$  and for the bachelor track. As the split tracks will be detected with almost the same momentum and the proton carries most of the momentum of the  $\Lambda$ , the relative momentum of the reconstructed  $\Lambda$  and the bachelor is almost zero. Then the invariant mass  $M$  is the sum of the rest masses  $m_i$ :

$$\begin{aligned}
 M^2 c^4 &= (E_p + E_\Lambda)^2 - (p_p + p_\Lambda)^2 c^2 \\
 &= E_p^2 + E_\Lambda^2 + 2E_p E_\Lambda - p_p^2 c^2 - p_\Lambda^2 c^2 - 2p_p p_\Lambda c^2 \\
 &= m_p^2 c^4 + m_\Lambda^2 c^4 + 2E_p E_\Lambda - 2p_p p_\Lambda c^2 \\
 &\approx m_p^2 c^4 + m_\Lambda^2 c^4 + 2(m_\Lambda^2 c^4 + p^2 c^2) - 2p^2 c^2 \\
 &\approx 4m_\Lambda^2 c^4,
 \end{aligned}$$

considering that the momenta  $p_i$  of the two particles are almost equal, except for some deviation due to the added pion. However to support the hypothesis of track splitting,  $\bar{\Lambda}$  were also combined with proton and the invariant mass does not have this spike (Figure 4.17): in this case the antiproton from the  $\bar{\Lambda}$  and the proton are well separated because they are bent away from each other due to the magnetic field. As the pion is in most of the cases a low momentum particle it can be separated with the PID of the TPC. At higher momentum of a pion can not be separated by the TPC from a proton, if then the track is split it can be identified as the bachelor proton and the pion from the  $\Lambda$ . But then the invariant mass distribution, of those candidates, is distributed over a wider and not peaked.

Despite the absence of a signal, the background can be studied further using event mixing or like-sign methods. A first attempt was made combining  $\bar{\Lambda}$  and proton which results in the distribution shown in Figure 4.17. The distribution of the invariant mass of  $\bar{\Lambda}$  and proton, and their antiparticles does not

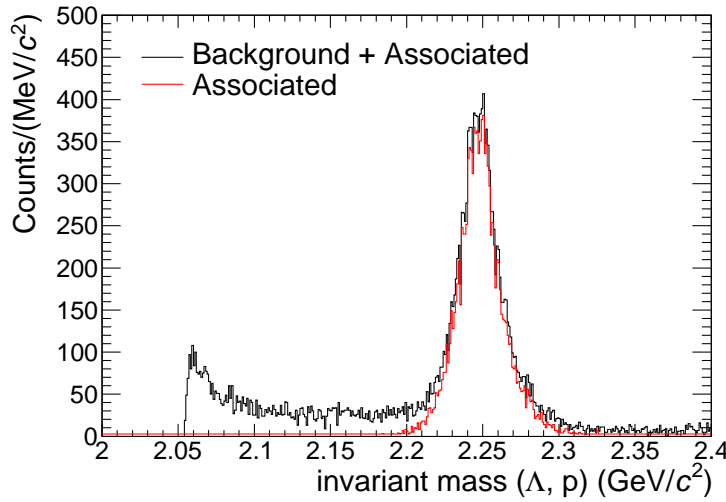


**Figure 4.14:** Invariant mass distribution of  $\Lambda$  and proton, and their antiparticles in Monte Carlo after applying the tightened selection criteria. The peak contains almost only associated dibaryons.

describe the background at small invariant mass as described above. In this distribution also no peak is visible.

---

### Efficiency

---

The efficiency in Monte Carlo is evaluated for the centrality range from 0 to 5% and depends mainly on the rapidity  $y$  and transverse momentum  $p_T$ , but also on the decay length of the particle, here it is assumed to be the same as for the  $\Lambda$ . A two dimensional plot for the efficiency depending on the rapidity and transverse momentum is shown in Figure 4.18. At low transverse momentum, below 3 GeV/c, the efficiency is a few percent or even less. In the region of the absolute rapidity above 0.6 the efficiency cannot be assumed to be constant as a function of rapidity as it first increases and drops then down. Therefore, the investigation of the efficiency is constrained to a window in the rapidity of  $y = \pm 0.6$ , since the efficiency will be integrated in  $y$ . It can be also noted that dibaryons with a momentum lower than 1.5 GeV/c are not detected (the injected ( $\Xi^0 p$ ) dibaryons are flat distributed in  $p_T$  from 0 to 10 GeV/c). The drop in the efficiency can be explained, since the  $\Lambda$  and proton both carry about half of the momentum of the dibaryon, as they have similar masses. After the decay of the  $\Lambda$  into proton and  $\pi$ , the proton takes a huge fraction of the momentum, leaving the  $\pi$  with not enough momentum to reach the TPC.

For the different selection criteria the efficiency changes as shown in Figure 4.19 with the corresponding selection criteria listed in Tables 4.4 and 4.5. The efficiency includes the branching ratio of the  $\Lambda$  decaying into proton and  $\pi^-$  of about 64%. The reconstruction efficiency per track and the  $V^0$  algorithm efficiency are included in the total efficiency. Those two efficiencies depend themselves on the transverse momentum for all three tracks. All the (grand-)daughters (two protons and one pion), are reconstructed in about 64% the cases, if the transverse momentum of the dibaryon is higher than 4 GeV/c. And the  $V^0$  algorithm has an efficiency of about 50% for the same transverse momentum of the dibaryon to find the secondary  $\Lambda$ . This results in an efficiency of about 32%. Any further reduction of the total efficiency is due to the selection criteria applied. Already with the reconstruction criteria the efficiency is reduced to less than 12%, resulting in the shown efficiencies.

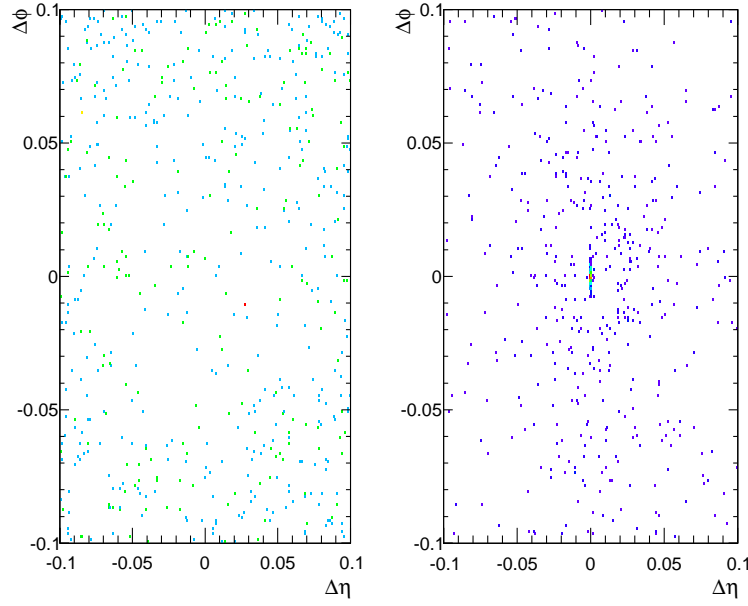


**Figure 4.15:** The distribution of the difference of the angles  $\phi$ , and  $\eta$  of the two proton tracks, used to reconstruct the dibaryon, is shown for dibaryons with a mass below  $2.1 \text{ GeV}/c^2$ . A peak at small angle differences is observed, which supports the thesis of track splitting.

Since the signal is not observed in data, an estimation of the expected amount of reconstructed dibaryons can be done integrated in transverse momentum, rapidity and centrality. For this purpose a weighted efficiency is needed, as the injected transverse momentum  $p_T$  is not realistic, because no detected particle has such a shape. The shape is assumed to be that obtained using the blast-wave parametrization [33]. The blast wave is a simplified approach of the hydrodynamics, which describes the collective expansion of the system created in heavy-ion collisions. The blast wave model has three parameters,  $\beta$ ,  $T_{fo}$ , and  $n$ . They are the velocity parameter, the kinetic freeze-out parameter and a scaling parameter. The model assumes a spectrum of pure thermal sources which are boosted in the transverse direction. Fitting the blast wave allows, with a few parameters, a phenomenological description of the spectra. With the parameters, extracted from a fit, the spectra of other particles with mass  $m_i$  can be approximated. To obtain the normalized  $p_T$  spectrum for the dibaryon, the parameters are taken from the fit to the spectra of deuteron and helium-3 in Pb-Pb collisions with ALICE, as these particles have similar masses. Using the supposed mass of the dibaryon of  $2.248 \text{ GeV}/c^2$  the shape of the spectrum shown in Figure 4.20 is obtained (red curve) and compared with the spectrum obtained for the  $\Lambda n$  bound state (blue curve) for which the same parameters have been used. The convolution of the efficiency with the blast wave fit gives the weighted efficiency, shown in the right panel of the same figure. The weighted efficiency is small, because the maximum of the blast wave is at the onset of the efficiency curve at  $p_T = 2 \text{ GeV}/c$ , whereas the maximum of the efficiency is at the tail of the expected  $p_T$  shape. The integrated weighted efficiency is  $9.9 \cdot 10^{-4}$  for the used criteria in central events. It should be noted that for the centrality range 0 to 80% the (weighted) efficiency might be higher. The number of expected dibaryons and antidibaryons is then estimated in the acceptance window using the thermal model prediction [11] as follows

$$N_{(\Xi^0 p)} = \underbrace{13.5 \cdot 10^6}_{\text{events}} \cdot \underbrace{9.9 \cdot 10^{-4}}_{\text{weighted eff.}} \cdot \underbrace{0.6}_{\text{BR.}(\Xi^0 p)} \cdot \underbrace{4.13 \cdot 10^{-3}}_{\frac{dN}{dy}} \cdot \underbrace{1.2}_{dy} \cdot \underbrace{2}_{\text{dibaryon+antidibaryon}} = 20$$

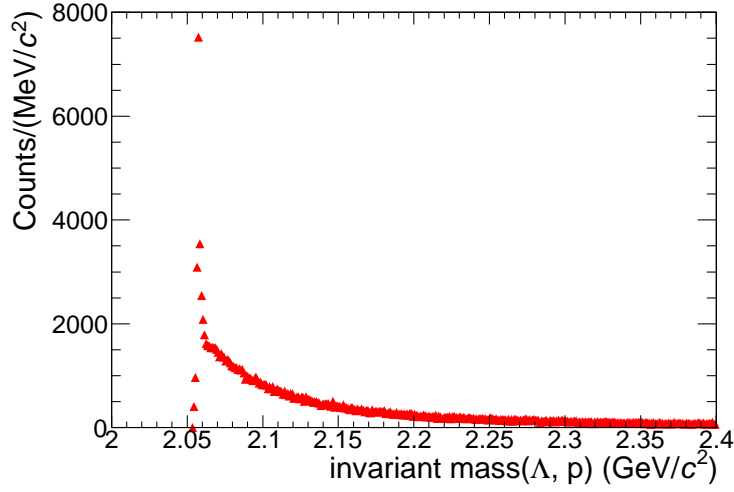


**Figure 4.16:** Invariant mass distribution of  $\Lambda$  and proton, and their antiparticles after applying the stronger selection criteria in 0-80% central Pb–Pb collisions at a center-of-mass energy  $\sqrt{s_{NN}} = 2.76$  TeV. A spike at  $2.06 \text{ GeV}/c^2$  is visible. The spike originates most likely from track splitting.

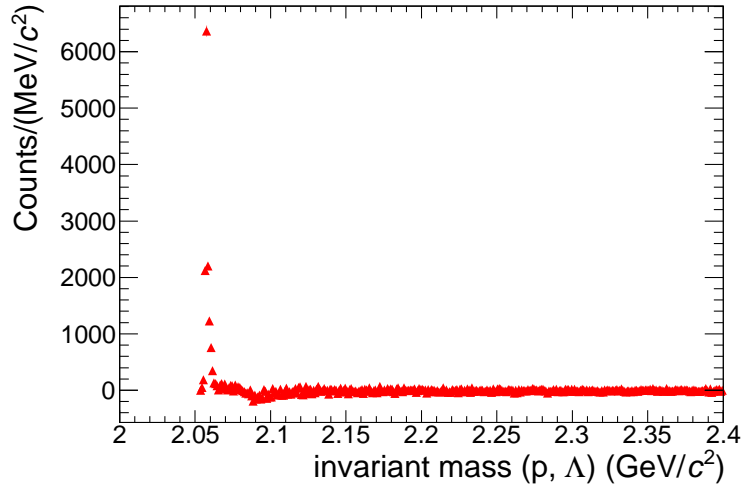


**Figure 4.17:** Invariant mass ( $\Lambda$ ,  $p$ ) distribution with the stronger selection criteria, after subtracting the invariant mass distribution of  $\bar{\Lambda}$  and proton, and their antiparticles.

For a significance  $sgn = \frac{S}{\sqrt{S+B}}$  of five and with the background  $B = 6213$  in a  $3\sigma$  window around the expected invariant mass the number of detected dibaryons and antibaryons would be

$$S = sgn \frac{sgn \pm \sqrt{sgn^2 + 4 \cdot sgn^2 B}}{2} \approx 407.$$

This is a factor twenty more than the expected signal. To set an upper limit for the production yield of the dibaryon we use a frequentist approach, which assumes a Poissonian likelihood distribution. The Frequentist approach means that the probability is defined as the limit of its relative frequency in a large number of events. The upper limit is then for the antibaryon  $\frac{dN}{dy} = 0.021$  with a confidence level of 0.99, see Table 4.6 for the other systems. The upper limit is above the prediction of the thermal model in central collisions ( $\frac{dN}{dydp} = 4.13 \cdot 10^{-3}$  for the centrality range from 0 to 10% for the  $(\Xi^0 p)$  dibaryon). For the centrality range from 0 to 80% with the thermal model estimated yield  $dN/dy$  has to be scaled down

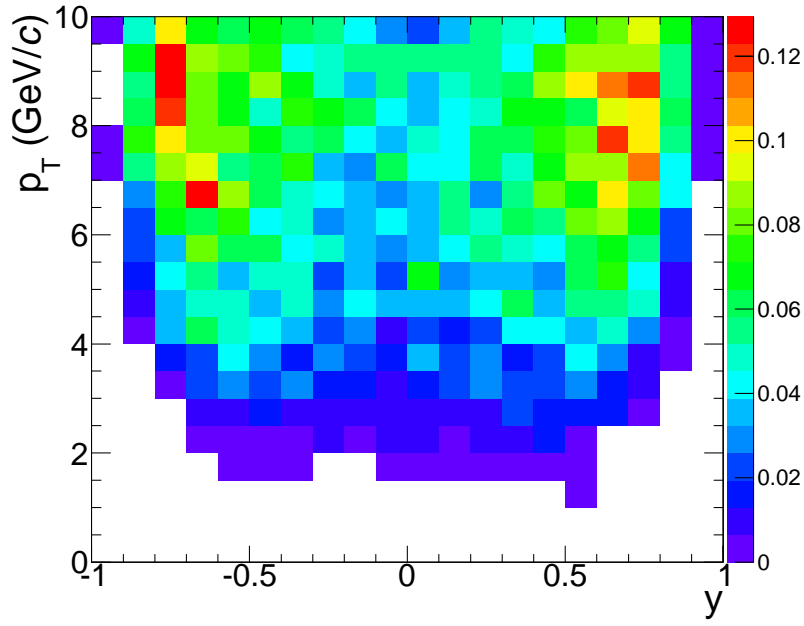


**Figure 4.18:** The efficiency shown as a function of the rapidity  $y$  and transverse momentum  $p_T$  for most central events.

by the number of participants, the factor is about 3.25, to be safe it can be compared to the yield of a fourth [34]. Then the predicted yield is reduced to  $dN/dy = 1.03 \cdot 10^{-3}$  for the  $(\Xi^0 p)$  dibaryon only. The prediction is an order of magnitude smaller than the upper limit, Figure 4.21.

#### 4.4 Effect of the lifetime on the efficiency

In the Monte Carlo production anchored to the Pb–Pb run in 2011 the lifetime of the dibaryon is reduced to  $c\tau = 4$  cm. For this sample the same tuned criteria are used, because the applied topological and kinematical criteria should not change, since they are independent of the lifetime, except the impact parameters may change. The invariant mass distribution of  $\Lambda$  and proton, and their antiparticles is built and the result is shown in Figure 4.22 for the centrality range from 0 to 80% for the same center-of-mass energy. The evaluated efficiency for this Monte Carlo simulation in the centrality range from 0 to 80% , Figure 4.23, has the same shape as before, but it is about a factor two higher than with the other lifetime of  $c\tau = 7.8$  cm and centrality range from 0 to 5%. This study has to be performed with different lifetimes and in different bins of the centrality, since the influences of the lifetime and of the centrality are not negligible.

**Table 4.4:** Main selection criteria used to reconstruct the  $(\Xi^0 p)$  dibaryon. In the last two column the fraction of kept signal and background for the optimized criteria compared to the reconstruction criteria are listed.

Selection criteria	reconstruction	optimized value	signal (%)	background (%)
IP in xy for $p_\Lambda$	$> 0.1$ cm	$> 0.4$ cm	96.4	62.4
IP in xy for $\pi_\Lambda$	$> 0.1$ cm	$> 1$ cm	97.7	80.1
DCA approach between $\Lambda$ daughters	$< 1$ cm	$< 0.4$ cm	91.9	48.1
IP in xy for $\Lambda$	$> 0.02$ cm	$> 0.2$ cm	90.0	68.3
$\cos(\theta_{p\Lambda}(\Lambda))$ wrt to prim vtx	$> 0.998$	$> 0.998$	-	-
$ \text{invariant mass}(p, \pi) - m_\Lambda $	$< 15 \text{ MeV}/c^2$	$< 8 \text{ MeV}/c^2$	98.0	55.6
IP in xy for $p_{\text{Bach}}$	$> 0.01$ cm	$> 0.3$ cm	94.3	71.8
DCA between dibaryon daughters	$< 1.5$ cm	$< 0.5$ cm	93.9	69.5
$\cos(\theta_{p\Lambda}(\Lambda))$ wrt to $(\Xi^0 p)$ vtx	$> 0.97$	$> 0.999$	99.2	92.6
$\cos(\theta_{p\Lambda}(\Xi^0 p))$ wrt to prim vtx	$> 0.97$	$> 0.999$	94.8	13.8
all criteria			40.2	0.6

**Table 4.5:** Used selection criteria to estimate the efficiency dependence on the criteria to select the  $(\Xi^0 p)$  dibaryon

Selection criteria	loose	tight
IP in xy for $p_\Lambda$	$> 0.4$ cm	$> 0.5$ cm
IP in xy for $\pi_\Lambda$	$> 1$ cm	$> 1.5$ cm
DCA between $\Lambda$ daughters	$< 0.3$ cm	$< 0.5$ cm
IP in xy for $\Lambda$	$> 0.1$ cm	$> 0.2$ cm
$\cos(\theta_{p\Lambda}(\Lambda))$ wrt to prim vtx	$> 0.998$	$> 0.998$
$ \text{invariant mass}(p, \pi) - m_\Lambda $	$< 8 \text{ MeV}/c^2$	$< 8 \text{ MeV}/c^2$
IP in xy for $p_{\text{Bach}}$	$> 0.3$ cm	$> 0.4$ cm
DCA between dibaryon daughters	$< 0.6$ cm	$< 0.4$ cm
$\cos(\theta_{p\Lambda}(\Lambda))$ wrt to $(\Xi^0 p)$ vtx	$> 0.9985$	$> 0.9995$
$\cos(\theta_{p\Lambda}(\Xi^0 p))$ wrt to prim vtx	$> 0.9985$	$> 0.9995$

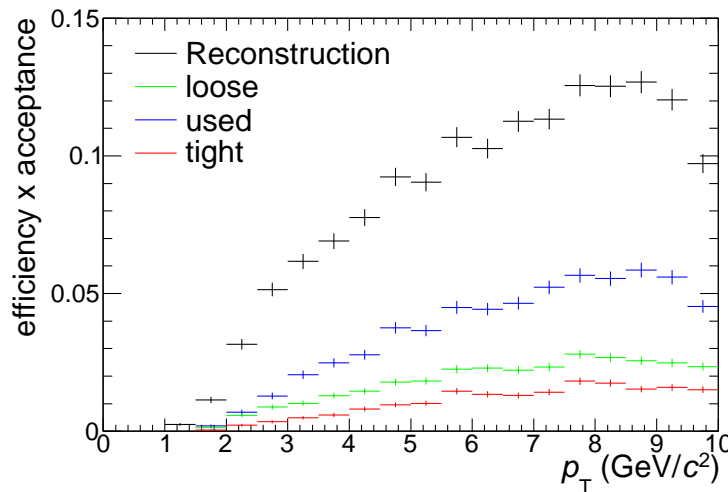


**Figure 4.19:** Efficiency obtained with the Monte Carlo simulation for the Pb–Pb events in 2010 and a lifetime of the dibaryon of  $c\tau \approx 8$  cm. Four different efficiencies for different sets of values for the selection criteria are shown. The sets are the reconstruction (black), the optimized (blue) and the optimized looser (green) and tighter (red).



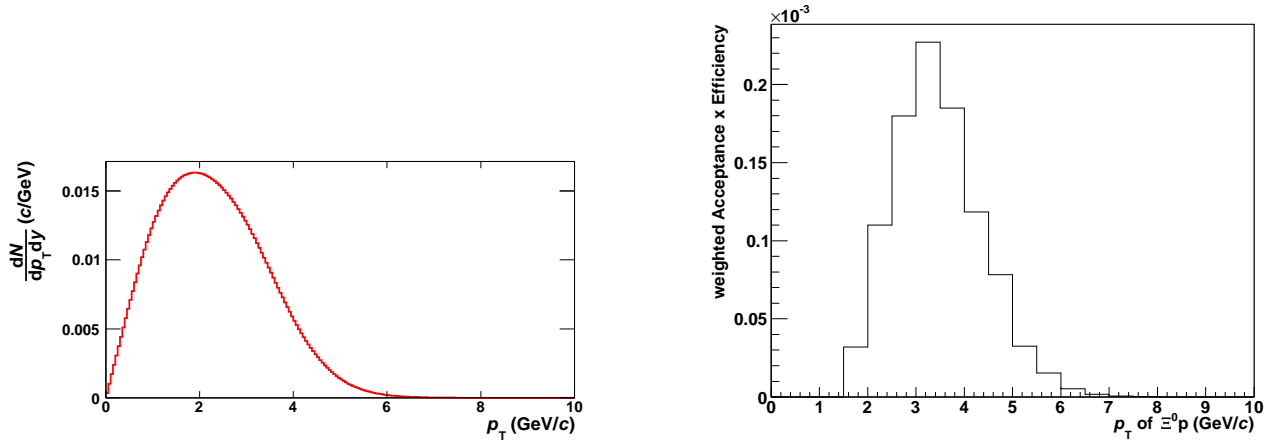


**Figure 4.20:** In the left panel are blast wave calculations shown for the  $(\Lambda n)$ ,  $(\Xi^0 p)$ , and H-dibaryon. In the right panel is the efficiency convoluted with the blast wave calculation for the  $(\Xi^0 p)$  dibaryon plotted.

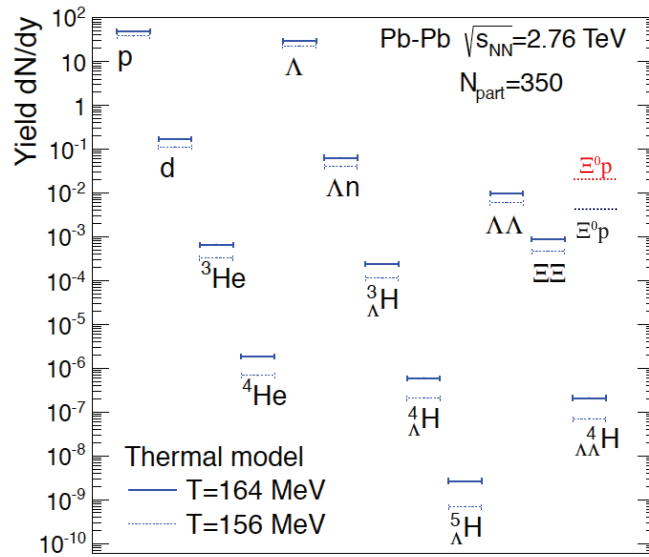


**Figure 4.21:** Production yield  $dN/dy$  from the thermal model (blue) for central Pb–Pb collisions and the upper limit  $dN/dy$  for the dibaryon (red) for the centrality range from 0 to 80%, obtained in this work.

**Table 4.6:** Upper production limits  $dN/dy$  for dibaryon, antibaryon and both together for a confidence level of 99%, with the number of counts in the expected signal region and the weighted efficiency.

	number of counts	weighted efficiency	upper limit $dN/dy$
antidibaryon	2970	$10.2 \cdot 10^{-4}$	0.21
dibaryon	3243	$9.5 \cdot 10^{-4}$	0.22
antidibaryon and dibaryon	6213	$9.9 \cdot 10^{-4}$	0.029

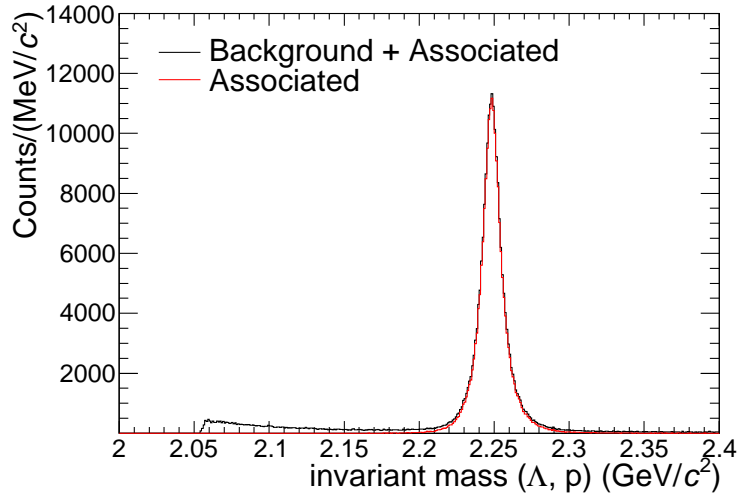


**Figure 4.22:** Invariant mass ( $\Lambda$ ,  $p$ ) distribution in Monte Carlo for 0-80% centrality in Pb-Pb events at a center-of-mass energy  $\sqrt{s_{NN}} = 2.76$  TeV with the selection criteria applied as obtained for the Pb-Pb run in 2010.

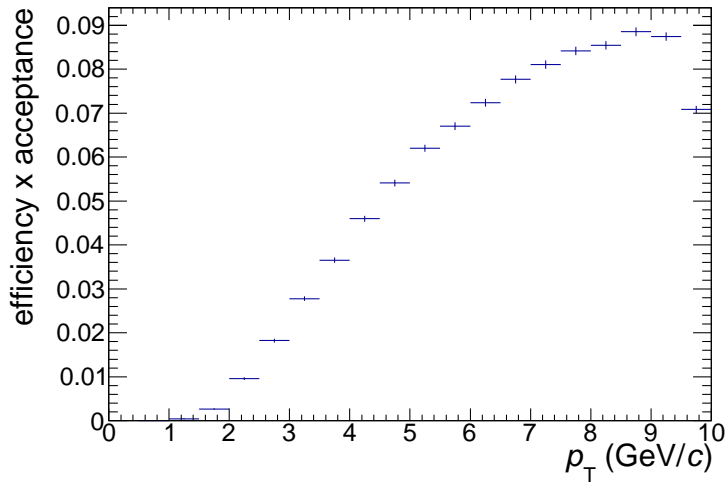


**Figure 4.23:** Efficiency with the Monte Carlo simulation for the data taken during the Pb-Pb run 2011 for the centrality range of 0 to 80% in Pb-Pb collisions at a center-of-mass energy  $\sqrt{s_{NN}} = 2.76$  TeV.

---

## 5 Conclusion and outlook

---

In this work, I presented an analysis to investigate the reconstruction of the proposed ( $\Xi^0 p$ ) dibaryon and its antiparticle. It was searched in the decay channel ( $\Xi^0 p$ )  $\rightarrow \Lambda + p$ . In the invariant mass distribution obtained with the data taken in the Pb–Pb run 2010 at a center-of-mass energy per nucleon pair  $\sqrt{s_{NN}} = 2.76$  TeV, no signal was observed in the centrality range from 0 to 80%. The reconstruction strategy is based on particle identification of the charged daughters of the dibaryons and on selection criteria related to topology and kinematic of the cascade decay. These criteria have been investigated by using a Monte Carlo production, in which the dibaryon is simulated. A peak at the lowest possible invariant mass was found. This peak was investigated and found to be most likely formed by split tracks. To further study the background  $\bar{\Lambda}$  and protons, and their antiparticles were also combined. Subtracting the invariant mass distribution from the invariant mass distribution of the dibaryon an almost flat distribution is obtained, with no visible signal.

An upper limit to the production yield was set by using the efficiency obtained with the Monte Carlo simulation and the transverse momentum distribution of the dibaryon estimated by using a blast-wave extrapolation from fits to measured deuteron and helium-3 spectra. The upper limit is calculated to be  $dN/dy = 0.029$  in the centrality range from 0 to 80%, for the dibaryon and antidibaryon together, compared with the predicted yield of the thermal model ( $4.13 \cdot 10^{-3}$  in central collisions) there is an order of magnitude difference, taking into account the lower production rate in collisions with less participants.

The same was started for 2011 Pb–Pb collision data and the corresponding Monte Carlo simulation for which the statistics is about a factor ten higher. The dependence of the result on the simulated lifetimes, binding energies and centrality has to be considered and studied. A background description with event mixing can be also investigated. If the signal is not observed, the upper limit would decrease as the statistics are higher and be below the prediction.



---

## List of Figures

---

2.1	Branching ratios of weakly decaying bound states versus the binding energy. . . . .	10
2.2	Production yields $dN/dz$ from the thermal model for central Pb–Pb collisions. . . . .	11
3.1	The LHC with its four large experiments . . . . .	13
3.2	Schematic picture of the accelerator system at CERN . . . . .	14
3.3	The ALICE detector system. . . . .	15
3.4	Specific energy loss $dE/dx$ measured with the TPC. . . . .	17
3.5	Schematic picture of the $\Lambda$ decay. . . . .	18
3.6	Schematic picture of the $\Xi^-$ decay and the $(\Xi^0 p)$ dibaryon decay . . . . .	19
4.1	In Monte Carlo reconstructed ionization signal of the TPC in the Monte Carlo sample . . .	22
4.2	Invariant mass distribution of $\Lambda$ and proton obtained with the reconstruction criteria in data	23
4.3	Invariant mass distribution of $\Lambda$ and proton obtained with the reconstruction criteria with the Monte Carlo sample . . . . .	25
4.4	Impact parameter of the $\Lambda$ daughters proton and pion . . . . .	26
4.5	Distance of closest approach between the $\Lambda$ daughters . . . . .	26
4.6	Impact parameter of the $\Lambda$ . . . . .	27
4.7	Cosine of pointing angle of the $\Lambda$ with respect to the primary vertex . . . . .	27
4.8	Invariant mass distribution of $\pi$ and proton . . . . .	28
4.9	Impact parameter of the bachelor proton . . . . .	29
4.10	Distance of closest approach between the $\Lambda$ and bachelor proton . . . . .	30
4.11	Cosine of pointing angle of the $\Lambda$ with respect to the dibaryon vertex . . . . .	30
4.12	Cosine of pointing angle of the dibaryon with respect to the primary vertex . . . . .	31
4.13	Normalized distributions of the cosine of pointing angle for the dibaryons and antidibaryon with respect to the primary vertex in different transverse momentum intervals (left panel) are shown. Invariant mass distributions of $\Lambda$ and proton, and their antiparticles for different transverse momentum intervals (right panel) are shown. . . . .	33
4.14	Invariant mass distribution of $\Lambda$ and proton and their antiparticles in Monte Carlo after applying the stronger selection criteria . . . . .	34
4.15	Opening angle between the proton tracks . . . . .	35
4.16	Invariant mass distribution of $\Lambda$ and proton, and of their antiparticles after applying the stronger selection criteria . . . . .	36
4.17	Invariant mass ( $\Lambda$ , p) distribution with the stronger selection criteria, after subtracting the invariant mass distribution of $\bar{\Lambda}$ and proton, and their antiparticles. . . . .	36
4.18	Efficiency versus rapidity and transverse momentum . . . . .	37
4.19	Efficiency obtained with the Monte Carlo simulation . . . . .	38
4.20	Blast wave predictions and the weighted efficiency times acceptance . . . . .	39
4.21	Production yield $dN/dy$ from the thermal model (blue) for central Pb–Pb collisions and the upper limit $dN/dy$ for the dibaryon (red) for the centrality range from 0 to 80%, obtained in this work. . . . .	39
4.22	Invariant mass ( $\Lambda$ , p) distribution in Monte Carlo for 0-80% centrality in Pb–Pb events at a center-of-mass energy $\sqrt{s_{NN}} = 2.76$ TeV with the selection criteria applied as obtained for the Pb–Pb run in 2010. . . . .	40
4.23	Efficiency with the Monte Carlo simulation for the data taken during the Pb–Pb run 2011 for the centrality range of 0 to 80% in Pb–Pb collisions at a center-of-mass energy $\sqrt{s_{NN}} = 2.76$ TeV. . . . .	40



---

## List of Tables

---

4.1	Event selection criteria . . . . .	21
4.2	Selection criteria and corresponding values used to reconstruct $V^0$ particles in the offline V0 finder. . . . .	23
4.3	Reconstruction criteria for the dibaryon . . . . .	24
4.4	Main selection criteria used to reconstruct the $(\Xi^0 p)$ dibaryon. In the last two column the fraction of kept signal and background for the optimized criteria compared to the reconstruction criteria are listed. . . . .	38
4.5	Used selection criteria to estimate the efficiency dependence on the criteria to select the $(\Xi^0 p)$ dibaryon . . . . .	38
4.6	Upper production limits $dN/dy$ for dibaryon, antidibaryon and both together for a confidence level of 99%, with the number of counts in the expected signal region and the weighted efficiency. . . . .	39





---

## Bibliography

---

- [1] J. Schaffner-Bielich, R. Mattiello and H. Sorge. Dibaryons with strangeness: their weak nonleptonic decay using SU(3) symmetry and how to find them in relativistic heavy-ion collisions. *Phys. Rev. Lett.*, 84:4305–4308, 2000.
- [2] Betty Bezverkhny Abelev et al. Multi-strange baryon production at mid-rapidity in pb-pb collisions at  $\sqrt{s_{NN}} = 2.76$  tev. *Phys.Lett.*, B728:216–227, 2014.
- [3] Betty et al. Abelev. Multi-strange baryon production in pp collisions at  $\sqrt{s} = 7$  TeV with ALICE. *Phys.Lett.*, B712:309–318, 2012.
- [4] K. et al Aamodt. Strange particle production in proton-proton collisions at  $\sqrt{s} = 0.9$  TeV with ALICE at the LHC. *Eur.Phys.J.*, C71:1594, 2011.
- [5] A. Andronic, P Braun-Munzinger and J. Stachel. Hadron production in central nucleus-nucleus collisions at chemical freeze-out. *Nucl.Phys.*, A772:167–199, 2006.
- [6] J. Beringer et al. (Particle Data Group. Particle Physics Booklet. *Phys. Rev. D*86, 010001, 2012.
- [7] T. Rijken, M. Nagels and Y. Yamamoto. Baryon-baryon interactions: the nijmegen extended-soft-core models. *Progress of Theoretical Physics Supplement*, 185:14–71, 2010.
- [8] J. Schaffner, C. Dover, A. Gal, C. Greiner and H. Stöcker. Strange hadronic matter. *Phys. Rev. Lett.*, 71:1328–1331, 1993.
- [9] Jürgen Schaffner, Carsten Greiner, and Horst Stöcker. Metastable exotic multihypernuclear objects. *Phys. Rev. C*, 46:322–329, Jul 1992.
- [10] P Braun-Munzinger, K. Redlich and J. Stachel. Particle production in heavy-ion collisions. 2003.
- [11] private communication with A. Andronic.
- [12] A. Wroblewski. Hypernuclei (and strange particles) – how it all began.
- [13] N. Martin. Master thesis, 2012.
- [14] C. Kuhn, B. Hippolyte, J. P. Coffin, J. Baudot, I. Belikov, D. Dietrich, M. Germain, and C. Suire. Search for strange dibaryons in star and alice. *Journal of Physics G: Nuclear and Particle Physics*, 28(7):1707, 2002.
- [15] R. Jaffe. *Phys. Rev. Lett.*, 38, 1977.
- [16] B. Doenigus for the ALICE Collaboration. (Anti-)matter and hyper-matter production at the LHC with ALICE. *Nucl. Phys. A* 904-905,547c, 2013.
- [17] N. Shah for the STAR Collaboration. Study of hyperon-hyperon correlations and search for the H-dibaryon with the STAR detector at RHIC, 2012.
- [18] Nicole Martin for the ALICE Collaboration. (anti-)matter and hyper-matter production at the lhc with alice. *Journal of Physics: Conference Series*, 455(1):012007, 2013.
- [19] Overall view of the LHC experiment. *Website*, 2013. [Online] [http://www.weltmaschine.de/sites/site\\_weltmaschine/content/e92/e70729/e70810/imageobject70817/9906026-A4-at-144-dpi.jpg](http://www.weltmaschine.de/sites/site_weltmaschine/content/e92/e70729/e70810/imageobject70817/9906026-A4-at-144-dpi.jpg).

- 
- [20] P. Bryant L. Evans. LHC Machine. *JINST*, 3:S08001, 2008.
- [21] Georges et al. Aad. Observation of a new particle in the search for the Standard Model Higgs boson with the ATLAS detector at the LHC. *Phys.Lett.*, B716:1–29, 2012.
- [22] S. Chatrchyan et al. Observation of a new boson at a mass of 125 GeV with the CMS experiment at the LHC. *Phys.Lett.*, B716:30, 2012.
- [23] A. Augusto Alves et al. The LHCb Detector at the LHC. *JINST*, 3:S08005, 2008.
- [24] G. Aad et al. The ATLAS Experiment at the CERN Large Hadron Collider. *JINST*, 3:S08003, 2008.
- [25] R. Adolphi et al. The CMS experiment at the CERN LHC. *JINST*, 3:S08004, 2008.
- [26] Overview of the Cern Accelerator complex. *Website*, 2013. [Online] <http://images.netzwelt.de/article/2011/nutzer-ab-sofort-experimente-rund-lhc-unterstuetzen-bild-cern7069.jpg>.
- [27] ALICE Collaboration. Technical Design Report of the Inner Tracking System . *CERN/LHCC 99-12*, 1999.
- [28] ALICE Collaboration. Technical Design Report of the Time Projection Chamber. *CERN/LHCC 2000-001*, 2000.
- [29] ALICE Collaboration. Technical Design Report on Forward Detectors: FMD, T0 and V0 . *CERN/LHCC 2008-014*, 2004.
- [30] H. Bethe. Zur Theorie des Durchgangs schneller Korpuskularstrahlen durch Materie. *Annalen der Physik*, 397(3):325, 1930.
- [31] ALICE Collaboration. Aliroot. *Website*, 2013. [Online] <http://svn.cern.ch/guest/AliRoot/trunk/>.
- [32] Root. *Website*, 2013. [Online] <http://root.cern.ch/drupal/>.
- [33] E. Schnedermann, J. Sollfrank and U. Heinz. Thermal phenomenology of hadrons from 200 A GeV S+S collisions. *Phys. Rev. C* 48, 2462, 1993.
- [34] private communication with N. Martin and B. Dönigus.

---

### **Eigenständigkeitserklärung**

---

Hiermit versichere ich die vorliegende Ausarbeitung ohne Hilfe Dritter nur mit den angegebenen Quellen und Hilfsmitteln angefertigt zu haben. Alle Stellen, die aus Quellen entnommen wurden, sind als solche kenntlich gemacht.

Darmstadt, den March 31, 2014

---

(Joachim M. Tscheuschner)